Thermalization and Many-body Localization

Liangsheng Zhang

A Dissertation
Presented to the Faculty
of Princeton University
in Candidacy for the Degree
of Doctor of Philosophy

Recommended for Acceptance
by the Department of
Physics
Adviser: Professor David Huse

September 2016

Abstract

This dissertation examines two topics in the area of quantum thermalization: thermalization of entanglement and the many-body localization phase transition. We first explore the dynamics of the entanglement entropy near equilibrium in two quantum-chaotic spin chains undergoing unitary time evolution. It is found that entanglement entropy relaxes slower near equilibration for a time-independent Hamiltonian with an extensive conserved energy, while such slow relaxation is absent in a Floquet spin chain with no local conservation law. We thus argue that slow diffusive energy transport is responsible for the slow relaxation of the entanglement entropy in the Hamiltonian system, and also attempt to make the relation more quantitative. We next turn to the many-body localization (MBL) transition, which is the quantum phase transition between the MBL phase, where localized conserved quantities emerge, and the thermal phase. We introduce and explore a Floquet spin chain model for numerical studies of this transition in finite-size systems. With no local conservation laws and rapid thermalization in the thermal phase, we argue that choosing a Floquet model can maximize contrast between the MBL phase and the thermal phase in such finite-size systems. Lastly, we present a simplified strong-randomness renormalization group (RG) that captures some aspects of the MBL phase transition in generic disordered one-dimensional systems and might serve as a "zeroth-order" approximation for future RG studies. This RG can be formulated analytically and is mathematically equivalent to a domain coarsening model that has been previously solved, which thus enables us to obtain the critical fixed point distribution and critical exponents analytically or to numerical precision. One interesting feature is that the rare Griffiths regions are fractal, which might be qualitatively correct beyond our approximation and suggest stronger Griffiths effects than previously assumed.

Acknowledgements

Obtaining PhD is an endeavor that could not be accomplished without help from other people. I am very glad to have such a great opportunity to explore the fascinating areas of physics at Princeton, which not only has a beautiful campus but also fantastic people to discuss intriguing ideas.

First and foremost, I would like to thank my advisor, Professor David Huse. It is David who transformed me from a student who just absorbed what is written in books to an explorer who tries to light his own way into the unknown. Attacking research problems at the edge of human knowledge can be intimidating and sometimes frustrating, but David is always available for guidance and encouragement. His ability to extract the essence and organize intricate details of any convoluted physics argument is remarkable, and I learned a lot from him on how to structure my thoughts and place vague ideas onto more concrete foundations, which has importance beyond just doing research. David is also supportive outside of academic life, and particularly he has helped me a lot on some of my visa applications, which usually tends to cause headache for international students.

My academic journey would be less colorful without my peers, and here I would like to give my thanks to my colleagues Hyungwon Kim, Bo Zhao and Trithep Devakul also in David's group, with whom I have had extensive collaboration on my research projects, and I really enjoyed sparkling discussions with them. I would also like to thank Professor Michael Romalis and Doctor Dong Sheng for their support and instruction during my experimental project. Without their aid, as a theorist who always lives with simplified ideals, I would not have had such a pleasant experience tasting a lab life with circuits and lasers where approximations tend to fail and appreciating the application of physics outside of papers.

Life at Princeton is not just about research. Random discussions were always tasty on the 4th floor in Jadwin Hall with my friends, including Bin Xu, Yu Shen,

Jun Xiong, Yangle Wu and many more, and I enjoyed the time with my meal buddies Akshay Kumar, Chaney Lin and Vedika Khemani, where interesting ideas were digested along with delicious food. I would like to thank my roommates Yu Song and Yang Xiu, without whom my living room would have just been empty and lonely, and also my high school and college friends Hao Zheng and Degang Wu for our years long exuberant discussions on physics and life.

Last but not the least, I must give special thanks to my family. The love and support from my parents are like trickling brooks, usually silent but never-ending. Without them, this dissertation would have just been an empty document.

To my parents.

Contents

List of Tables

List of Figures

Chapter 1

Introduction

Thermal phenomena are ubiquitous in our daily life: they represent most of our experience dealing with macroscopic objects in nature. The study of our thermal experience begins with the investigation of macroscopic objects at thermal equilibrium based on Newtonian mechanics. The main challenge of any analysis of macroscopic objects with $\mathcal{O}(10^{23})$ constituent particles lies in the vast amount of information we have to deal with if we would like to track the movement of every particle. To circumvent this problem, statistics is brought into the subject so instead of considering the full trajectories of every particle, we only focus on a few average quantities which we believe characterize the equilibrium properties of the system. The study of phenomenological relations between these average quantities constitute much of thermodynamics, and the "derivation" of these quantities from microscopic descriptions of the system based on the statistical idea of ensemble and the use of partition function becomes the subject of statistical mechanics. Furthermore, as quantum theory gradually replaces Newtonian theory to become the underlying description of states of particles, it is also natural to incorporate quantum mechanics into traditional statistical mechanics which gives it power to examine less traditional macroscopic objects

like superconductors. With thermodynamics and statistical mechanics, many thermal equilibrium phenomena of macroscopic objects can find satisfactory explanations.

However, technically nothing really reaches perfect equilibrium: most objects that are of interest to us are constantly perturbed by external stimulus and thus always evolving. Our current technologies also rely more on objects being moving rather than static. Therefore a proper understanding of dynamical properties is of great importance and in the meantime also more difficult, as it becomes less easy to escape the microscopic details of the system. Moreover, the study of dynamical process of reaching thermal equilibrium seems to challenge our notions of describing thermal equilibrium using a only few macroscopic quantities. Since quantum mechanics assumes unitary dynamics which preserves all the information from initial conditions, it is natural to expect to reach different equilibrium states starting from different initial states. The success of description of final equilibrium with only a few macroscopic variables, which contain much less information than initial states, thus creates a paradox in our understanding. The investigation of this thermalization process, and more importantly, when it fails, has become a hot topic in recent years.

In the remaining sections of this chapter, we will briefly review some important concepts in our understanding of the thermalization process and the many-body localization, a generic phase of matter which fails to reach thermal equilibrium.

1.1 Thermalization

1.1.1 Closed System Quantum Mechanics

In traditional statistical mechanics, we usually start with a microcanonical ensemble of an isolated system: these are considered "simple" cases as no environmental effects have to be taken into consideration. In the quantum mechanical arena, closed quantum system can be described by a normalized vector $|\psi\rangle$ in a Hilbert space,

which represents full information contained in it. With n particles each having $s > 1$ states, the Hilbert space is of dimension s^n, which can be enormous when we are confronted with macroscopic objects in statistical mechanics where $n \sim \mathcal{O}(10^{23})$. As mentioned above, we introduce statistics to cope with this astronomical number and this is implemented in quantum mechanics by using a density matrix ρ which satisfies the following properties:

$$\rho^\dagger = \rho\,, \quad \mathrm{Tr}\rho = 1\,, \quad \rho \geq 0 \tag{1.1}$$

where the last condition means it is positive semi-definite. Generically, the density matrix can be written as

$$\rho = \sum_i p_i |\psi_i\rangle\langle\psi_i| \tag{1.2}$$

with $1 \geq p_1 \geq p_2 \geq \cdots \geq 0$ and an orthonormal basis $\{|\psi_i\rangle\}$. If $p_1 = 1$ then $p_i = 0$ for $i \geq 2$ and the density matrix in this case represents a pure state in Hilbert space. In other cases, the density matrix represents a probabilistic mixture of different states and our ignorance of the exact state that the system is in, which is the reason that the density matrix representation is useful in the formulation of quantum statistical mechanics. The dynamics of the system is generated by a time independent Hamiltonian H. If we are in the Schrödinger picture, the time evolution of the system is represented by the evolution of the density matrix:

$$i\hbar\frac{d\rho}{dt} = [H, \rho] \tag{1.3}$$

and at any time t, the measurement of a time independent operator O generates an expectation value $\mathrm{Tr}\{O\rho(t)\}$.

One class of operators that receives special attention in studies of thermalization are few-body or local operators which usually have local support in real space on the

system, where the fraction of support vanishes under thermodynamic limit. Particularly, the Hamiltonian H is usually a sum of local operators, and we only consider extensive conserved quantities which are also sums of local operators. With this constraint, a generic system may have only a few (compared to the dimension of the pure state Hilbert space) conserved quantities, even though the Hamiltonian itself can commute with many more independent "global" operators like the projector to one of its eigenstates. Moreover, the densities of conserved quantities can only be transported locally, because of the locality of H.

Another interesting point to note is that the solution of Eq. (1.3) can be written as

$$\rho(t) = U(t)\rho(0)U(t)^\dagger \tag{1.4}$$

with unitary operators $U(t) = \exp(-iHt)$. A natural generalization of this dynamics would be to use other unitary operators which are not naturally generated by some Hamiltonian. A usual requirement on these unitary operators is to have their operations on the system be local, since $U(t)$ is generated by a Hamiltonian H which only acts locally. One particular class of these unitary operators that is of interest is Floquet operators, which can be thought of being generated by time-dependent Hamiltonian with period τ so that $H(t+\tau) = H(t)$. Usually we just sample the state of the system at discrete times (stroboscopic time) $n\tau$ with integer n. The reason we consider Floquet systems is that they have no conserved energy density [2] and in fact we can construct Floquet systems that have no conserved densities at all. Technically speaking, under this Floquet dynamics the system is no longer isolated as in practice we would require external force to periodically drive the system. Nevertheless, we can still conceptually interpret it as providing an alternative dynamics to the closed quantum system which can become useful particularly in numerical studies.

1.1.2 Quantum Thermalization

We are now ready to give a more precise description of the thermalization process under quantum mechanics. Below we will define the process using subsystems and thus canonical ensembles as in Ref. [2]. One can also directly consider the whole isolated system and thus microcanonical ensemble as in Ref. [3].

We consider an isolated quantum system which cannot be further divided into more closed systems. This system (or more precisely the space of degrees of freedom) is partitioned into two parts: a subsystem S and its bath B so that the total system's Hilbert space is $H_F = H_S \otimes H_B$. To study thermalization, we need to take the thermodynamic limit, and in this description it means adding more degrees of freedom in B but keeping those in S fixed, which will result in an unbounded number of degrees of freedom added to the whole system. On considering this process, we will focus on initial states which change as needed as we add more degrees of freedom, and describe them as $\rho_N(t = 0)$ where N represents the total number of degrees of freedom in the whole system. To have a well-defined thermal equilibrium in this limit, all these initial states should thermalize to same values of intensive variables which are conjugate to the conserved extensive quantities. An example is the temperature T which is conjugate to the conserved energy $\langle H \rangle$. Particularly, this constrains the average densities of these conserved quantities in this process, and requires their variance to grow no faster than the volume of the system, i.e., the usual $\sqrt{N}$ deviation we have in statistical mechanics. Otherwise, this requirement does not impose any constraint on the distribution of these densities which can take the system far from thermal equilibrium.

At each N, the initial state evolves according to Eq. (1.3) for the whole system and at any time t the subsystem can be characterized by a reduced density matrix

by taking a partial trace over the degrees of freedom in B:

$$\rho_S^N(t) = \mathrm{Tr}_B \rho(t)\,. \tag{1.5}$$

On the other hand, according to the canonical ensemble, there is a density matrix ρ^{eq} given by the set of intensive variables describing the thermal equilibrium of the full system. For example, when there is only energy conservation so that the thermal equilibrium is given by a temperature T, we have an equilibrium density matrix

$$\rho^{eq} = \frac{1}{Z(T)} \mathrm{e}^{-\frac{H}{k_B T}} \tag{1.6}$$

where $Z(T) = \mathrm{Tr}\exp(-H/k_B T)$ is the partition function. The corresponding subsystem S at this equilibrium is thus described by $\rho_S^{eq} = \mathrm{Tr}_B \rho^{eq}$. For a Floquet system with no conserved densities, ρ_S^{eq} would just be the identity operator on S up to some normalization factor. Note the Hamiltonian implicitly has the parameter N as it is constructed given a fixed N, so ρ_S^{eq} also implicitly depends on N. The whole system is considered to thermalize if for any subsystem S that satisfies the property given above [4–7]:

$$\lim_{t\to\infty} \lim_{N\to\infty} \rho_S^N(t) = \lim_{N\to\infty} \rho_S^{eq}\,. \tag{1.7}$$

The two limits on the left hand side have to be taken together: at finite N, $\rho_N(t)$ would be quasi-periodic and thus has no limit under $t \to \infty$, while at finite t, because of our requirements of local operators above, all imbalance of densities of conserved quantities relative to thermal equilibrium distributions can only be transported for a finite distance, so large enough system would not reach thermal equilibrium.

Defining thermalizing process above can resolve the paradox between "missing information" of initial conditions under thermalization and the preservation of information under unitary evolution in quantum mechanics: the (local) information is

not erased but just hidden from (small) subsystems. Particularly, we can only perform local operations so at most only local properties about initial conditions can be extracted. At long time, each subsystem gets heavily entangled with the whole system so the initial local information becomes inaccessible from local operations, and thus appears erased for the performer of local operations. This manifests itself in our definition that ρ_S^{eq} is derived from ρ^{eq} which contains no local initial information compared to the true density matrix of the whole system ρ_N.

1.1.3 Eigenstate Thermalization Hypothesis

Our macroscopic world experience tells us that most generic systems thermalize, and if a system does thermalize to a set of intensive variables, then it thermalizes under a lot of initial states with the same conserved densities, and in fact, it seems all initial states under the constraint would thermalize. If indeed all initial states are thermalized, then all many-body eigenstates of the Hamiltonian H should also thermalize, which is known as the Eigenstate Thermalization Hypothesis (ETH) [4–7]. For Floquet systems, we instead consider the eigenstates of $U(\tau)$ which evolves the system by a full period τ. Unlike Hamiltonian eigenstates, these states are not stationary but periodic with period τ. To state the ETH more precisely, we consider an eigenstate of the Hamiltonian $H|n\rangle = E_n|n\rangle$ whose energy E_n corresponds to temperature T_n at thermal equilibrium. The density matrix of the whole system at any time is just $\rho = |n\rangle\langle n|$ and the subsystem S has reduced density matrix $\rho_S = \mathrm{Tr}_B\{|n\rangle\langle n|\}$. According to our definition of thermalization, in the thermodynamic limit, $\rho_S = \rho_S^{eq}$, the thermal density matrix of the subsystem from canonical ensemble at temperature T_n. This motivates a single-eigenstate ensemble of the full system, which can be viewed as a limiting case of microcanonical ensemble where the energy window is reduced to contain only one eigenstate, and it would behave as any other traditional statistical mechanics ensemble and give the correct thermal properties of subsystems

if the ETH holds. One consequence of the ETH is the "volume law" scaling of the entanglement entropy in an eigenstate when $T_n \neq 0$. Particularly, the entanglement of entropy of the subsystem S is defined as the von Neumann entropy

$$S_A = -\mathrm{Tr}\{\rho_S \log \rho_S\}\,, \tag{1.8}$$

and its extensive part in thermodynamic limit is expected to equal to the thermal entropy of subsystem S, which is proportional to its volume when $T_n \neq 0$.

With the ETH, we can view thermalization as a process of "dephasing" of off-diagonal terms in full system density matrix. Specifically, for a given initial state $\rho(t=0) = \sum_{n,m} \rho_{nm}|n\rangle\langle m|$ written in eigenstate basis $\{|n\rangle\}$ from the Hamiltonian, the density matrix of the full system at later time t is

$$\rho(t) = \sum_{n,m} \mathrm{e}^{-i(E_n - E_m)t/\hbar} \rho_{nm}|n\rangle\langle m| \tag{1.9}$$

which only has exponential time factors $\exp(-i(E_n - E_m)t/\hbar)$ for off-diagonal terms $n \neq m$. As $t \to \infty$, these phase factors become essentially random, so in the computation of average values of any local observable, the contribution from these off-diagonal terms would be almost zero, and this is called dephasing. Effectively in terms of local observables we can think of our system as in a "diagonal" ensemble at long time:

$$\rho_D = \sum_n \rho_{nn}|n\rangle\langle n|\,. \tag{1.10}$$

Since our initial state would have a set of given densities of conserved quantities with vanishing (relative to system size) fluctuations, in the thermodynamic limit the diagonal ensemble would only contain eigenstates with same densities of conserved quantities, and thus all of them contribute to the desired ρ_S^{eq} for any subsystem S with vanishing fraction relative to the full system size. Technically, to really have

zero contributions from off-diagonal terms, we would also need to require the local observables considered to have vanishing coupling between distinct eigenstates under thermodynamic limit [7, 8].

The ETH is not true for a broad class of systems, in which case the thermalization may also fail. One generic case where both the ETH and thermalization fail is many-body localized systems, which we will discuss in the next section. Another interesting case is that of integrable systems, where the number of conserved extensive quantities is of $\mathcal{O}(N)$, the total number of degrees of freedom. It is conjectured that integrable systems thermalize to the generalized Gibbs ensemble [9] described as

$$\rho_G = \frac{1}{Z} \mathrm{e}^{-\sum_n \lambda_n I_n}, \tag{1.11}$$

which can also be thought of as the maximum entropy ensemble [10] with $\mathcal{O}(N)$ constant of motions I_n and the corresponding Lagrange multipliers λ_n. This ensemble is different from the usual Gibbs ensemble as the latter has only $\mathcal{O}(1)$ number of constant of motions under the thermodynamic limit. One subtlety here, however, is how to choose these constants of motions, as choosing all (including non-local) conserved quantities would just make the ensemble trivial [3]. Motivated by standard assumption of statistical independence between subsystems in the construction of usual Gibbs ensemble, we may choose constants of motions which are at least approximately additive for small subsystems [11]. Integrable systems also have their own version of the ETH [12].

For systems where the ETH seems to hold, it is also difficult to either prove it analytically or have a thorough numerical test as it requires an extrapolation to the thermodynamic limit. On the other hand, in the usual case of successful thermalization, it seems we do not need the strong statement where all eigenstates thermalize; instead it is suffice if almost all eigenstates thermalize, and the latter has gained much

numerical support [7, 8, 13–23]. However, if there are some eigenstates which violate the ETH in any case where as a whole the system still thermalizes, it then raises a question about what are special about these rare eigenstates.

1.2 Many-body Localization

As mentioned in the previous chapter, there are situations where the ETH and thermalization fail, and a large class of them can be characterized as localized systems. The concept of localization was introduced by Anderson [24] and applies to systems with disorder, which usually manifests itself as random terms in the Hamiltonian or Floquet time evolution operator. Therefore when we are talking about properties of these models, we usually mean average properties which are averaged over different configurations of disorders. Many-body localization refers to interacting many-body systems with disorder, and on this topic we are interested in highly-excited states which are at energy densities corresponding to non-zero temperatures if the system ever thermalized.

1.2.1 Single-particle Localization

Before entering the world of disorder with interaction, we will first look at a non-interacting model with localization as in Ref. [2], which is a tight-binding model with hopping on an infinite lattice:

$$H = t \sum_{\langle ij \rangle} (c_i^\dagger c_j + c_j^\dagger c_i) + \sum_i U_i c_i^\dagger c_i \,, \tag{1.12}$$

where t controls nearest-neighbor hopping and U_i is a random potential. This model is written in a second quantization form so that $c_i^\dagger$ creates a particle at site i and c_i annihilates one. The Hamiltonian is essentially a single-particle Hamiltonian and

admits single-particle eigenstates of two forms: one is localized and the other is extended. A localized wavefunction has the asymptotic long distance form

$$\psi_\alpha(\vec{r}) \sim \mathrm{e}^{-|\vec{r}-\vec{R}_\alpha|/\xi}\,, \tag{1.13}$$

where ξ is the localization length and $\vec{R}_\alpha$ represents the center position that the particle is localized about. An extended wavefunction would just have the asymptotic long distance form $|\psi| \sim 1/\sqrt{V}$ where V is the volume of the whole system, and this wavefunction "covers" all sites. A particle starting from a wave packet would have diffusive dynamics if the wave packet is composed of extended eigenstates. In one or two dimensions, all eigenstates are localized, and in three or more dimensions, eigenstates would be localized with strong enough disorder, i.e., large variance of U_i. Particularly, in three or more dimensions, there could be a transition between extended states and localized states in the energy spectrum, which defines a "mobility edge". There are special critical states at the edge which display power-law instead of exponential (as in Eq. (1.13)) localization. As the disorder strength gets stronger, the single-particle eigenstates become strongly localized so that ξ in Eq. (1.13) is smaller than or on the order of a lattice spacing. This happens when $|t_{ij}| \ll |U_i - U_j|$ for almost all adjacent pairs. Since one can think of U_i and U_j as energies of particles exactly on site i and j, and t_{ij} is the hopping between these two sites, from a perturbation theory point of view, the true eigenstates would have some hybridization between sites i and j, and when $|t_{ij}/(U_i - U_j)| \ll 1$, the amplitude of hybridization is small, thus the eigenstate would just be localized around one site.

One can directly write out the many-body eigenstate of Eq. (1.12) by building up the Fock space. If a system has at least some localized single-particle eigenstates, then almost all of its many-body eigenstates violate the ETH and the system would not thermalize when these eigenstates are involved. For example, if the system starts

with a spatially non-uniform density of particles in localized states on a large length scale, then the inhomogeneity would not diffuse away as the localized states would only move around on a length scale $r \lesssim \xi$, and thus the system does not reach thermal equilibrium. Therefore, these disordered single-particle systems provide us a first glance at how localization breaks thermalization.

1.2.2 Many-body Localization: A Spin Model

To obtain an interacting localized systems, one can directly add interaction terms in Eq. (1.12) or similar single-particle disorder Hamiltonian. It can be shown from the perturbation theory that the many-body localization (MBL) of particles from a single-particle Hamiltonian can survive a weak enough interaction at non-zero temperatures [25], and this conclusion can also be generalized to infinite temperature [26]. In this section, we will briefly review some basic properties of MBL by looking at a spin model from Ref. [13]:

$$H = \sum_i \left(\vec{S}_i \cdot \vec{S}_{i+1} + h_i S_i^z \right) \tag{1.14}$$

where $S_i = \sigma_i/2$ and σ_i are the Pauli matrices for spin-1/2 at site i, and h_i are random magnetic fields with uniform distribution on $[-h, h]$.

At $h = \infty$, the many-body eigenstate is just a product state of up and down spins in z direction at each site. This state is trivially localized as each "particle", i.e., spin, is localized at one site. Around $h = \infty$, we can understand many-body eigenstates using perturbation theory. Particularly, as in the argument of strong disorder in Sec. 1.2.1, the typical level splitting between neighboring sites, i.e., $|h_i - h_j|$, is much larger than interactions which is 1 in Eq. (1.14), so spins at different sites are typically only weakly hybridized. This leads to the absence of DC spin transport and energy transport at strong disorder $h \gg 1$, and thus the lack of quantum thermalization from perturbation theory [25]. Numerical evidence has suggested that eigenstates of

(1.14) violate the ETH even in the region where the perturbation theory is no longer applicable, and the ETH is recovered only when $h \lesssim 3.5$ [13]. This demonstrates a quantum phase transition at some critical disorder strength, i.e., the magnitude of h, which separates the thermal phase, where eigenstates follow the ETH and the system theramlizes, from the localized phase, where the ETH breaks down and the system no longer thermalizes. This is an eigenstate phase transition as during the transition, the properties of eigenstates have a sharp change, thus leading to changes of the dynamics of the system. Around the transition point, it is also possible that only some but not all eigenstates are localized, thus creating a mobility edge [25], which leads to a more complicated behavior. In particular, statistical properties may be changed by rare regions in a localized state with a local energy density close to that of a mobility edge, which would generate some Griffiths phenomena [2].

Another point worth mentioning for MBL is the spread of quantum entanglement. Even though a localized system has zero DC conductivity, entanglement does get spread to the whole system as in a thermalized system. This can be easily seen from a simple two-spin version of (1.14) with interaction being J instead of 1:

$$H = J\vec{S}_1 \cdot \vec{S}_2 + h_1 S_1^z + h_2 S_2^z \tag{1.15}$$

If we start with a general non-entangled product sate

$$|t=0\rangle = (\alpha|\uparrow_1\rangle + \beta|\downarrow_2\rangle) \otimes (\gamma|\uparrow_2\rangle + \delta|\downarrow_2\rangle)\,, \tag{1.16}$$

then at any later time the state becomes (in the units where $\hbar = 1$)

$$\begin{aligned} |t\rangle =& \mathrm{e}^{-ih_1 t}\alpha|\uparrow_1\rangle \left(\mathrm{e}^{-i(h_2+J)t}\gamma|\uparrow_2\rangle + \mathrm{e}^{i(h_2+J)t}\delta|\downarrow_2\rangle\right) \\ &+ \mathrm{e}^{ih_1 t}\beta|\downarrow_1\rangle \left(\mathrm{e}^{-i(h_2-J)t}\gamma|\uparrow_2\rangle + \mathrm{e}^{i(h_2-J)t}\delta|\downarrow_2\rangle\right)\,. \end{aligned} \tag{1.17}$$

Except at certain special times, the state is no longer a product state and thus the system gets entangled without any transport of energy. Qualitatively, the entanglement is generated by precession of both spins, and the rate of precession depends on the interaction with the other σ_i^z. Quantitatively, the two eigenvalues of ρ_2, the reduced density matrix of spin 2, are

$$\lambda_\pm = \frac{1 \pm \sqrt{1 - 4|\gamma\delta|^2[1 - (|\alpha|^2 - |\beta|^2)^2]\sin^2(2Jt)}}{2} \tag{1.18}$$

so the von Neumann entropy $S = -\lambda_+ \ln \lambda_+ - \lambda_- \ln \lambda_-$ has a time scale $t \sim 1/J$, which only depends on the interaction between two spins. On the other, the spread of entanglement does distinguish the MBL systems from either general, i.e., non-integrable, thermal systems or integrable systems. In integrable one-dimensional systems, the entanglement spreads ballistically [27–29], i.e., an increase of entanglement entropy linear in time, and this is also observed, at least when far away from equilibrium, in one dimensional diffusive non-integrable models [30]. For localized models, however, the entanglement has been shown to spread logarithmically with time [28,31–38], thus much slower than that in thermal or integrable systems. We will explore the spread of entanglement further in the next section.

1.2.3 Many-body Localization: A Phenomenology

We may understand fully many-body localized (FMBL) systems, where all eigenstates display localization, better by rewriting Hamiltonian using "dressed" local operators from bare local operators [38]. Specifically, we can consider a system with only local two-state degrees of freedom like spins on a lattice and there are only short-range interactions between these degrees of freedom in the Hamiltonian. Operators on each local two-state degree of freedom i are thus a linear combination of the identity matrix I_i and the Pauli matrices $\vec{\sigma}_i$, which will be referred to as the "p-bits" (p=physical).

In the localized phase, since the system does not admit transport, there should be a set of localized conserved charges acting as constants of motion, and we may re-write Hamiltonian of the system in terms of the corresponding local operators. Particularly, it has been argued that [36–38] for FMBL systems, we can define a set of localized two-state degrees of freedom with corresponding Pauli operators $\vec{\tau}_i$ such that the Hamiltonian can be re-written as

$$H = E_0 + \sum_i \tau_i^z + \sum_{ij} J_{ij}\tau_i^z\tau_j^z + \sum_{n=1}^{\infty}\sum_{i,j,\{k\}} K^{(n)}_{i\{k\}j}\tau_i^z\tau_{k_1}^z\cdots\tau_{k_n}^z\tau_j^z\,, \tag{1.19}$$

where E_0 is some constant energy offset and no duplicate term is included. $\{\vec{\tau}_i\}$ generate the constants of motion and will be called "l-bits" (l=localized) in the following. The subscript i for l-bits refers to different degrees of freedom compared to the subscripts for p-bits, though for weakly interacting systems, $\vec{\tau}_i$ should have substantial overlap with $\vec{\sigma}_i$ and thus can be viewed as "dressed" p-bits, with the "dressing" falling off exponentially in the space of degrees of freedom from p-bits, which would be called real space for simplicity in the following. The interactions J_{ij} and $K^{(n)}_{i\{k\}j}$ in Eq. (1.19) also fall off exponentially in real space. Even though in terms of p-bits the Hamiltonian may only couple nearby ones, Eq. (1.19) allows long-range interaction between l-bits, as each of p-bits may have non-zero weight on distant l-bits.

Eigenstates of (1.19) are simultaneous eigenstates of all the $\{\tau_i^z\}$, thus as in Eq. (1.17) each l-bit would also precess about its z-axis at a rate given by its interactions with other τ_i^z. Therefore in a generic case, as in (1.17), different l-bits would get entangled during precession, but since there is no "flip" of $\{\tau_i^z\}$, there would be no "dissipation". Eq. (1.19) can also help us gain some understanding of the logarithmic spreading of entanglement in FMBL systems [36, 38]. On one extreme, for thermalizing systems, when entanglement is generated between two p-bits A and B through direct interaction and similarly between B and another p-bit C,

A and C would also get entangled during the process even though they may not directly interact. As a result, entanglement can spread ballistically in thermalizing systems [30]. On the other extreme, for single-particle localized systems, which do not have interactions between l-bits in (1.19), entanglement would not be generated between any l-bits through dynamics. FMBL systems are in the middle of these two extremes. With interaction, entanglement does get spread as is seen from Eq. (1.17). However, entanglement propagates much slower as it can only be generated by direct interaction between two l-bits. Intuitively, this is because the interaction between l-bits depend only on their τ^z values, which, as constants of motion, are not affected by a third l-bit, thus the interaction between two l-bits would not be "felt" by any third l-bit, and so is the entanglement generated from the interaction. More specifically, we can define the effective interaction between two l-bits i and j as

$$J_{ij}^{eff} = J_{ij} + \sum_{n=1}^{\infty} \sum_{\{k\}} K_{i\{k\}j}^{(n)} \tau_{k_1}^z \cdots \tau_{k_n}^z \,, \tag{1.20}$$

which would also depend on all the other $\{\tau_k^z\}$. In localized systems, we expect an exponential decay of J^{eff} as $J^{eff} \sim J_0 \exp(-L/\xi)$ with distance L between l-bits i and j. (The position of l-bits may be not straightforward to find since they are "extended". For weak interactions, l-bits can be thought of locating at their "undressed" p-bits.) If these two l-bits are initially not entangled, the entanglement is generated between them at $t \sim 1/J^{eff}$, analog to what happens with the state (1.17). Therefore, after time t, entanglement is generated for l-bits within $L \sim \xi \ln(J_0 t)$, so the entanglement grows logarithmically in time.

We close this section by mentioning again that the l-bit reasoning here applies for fully many-body localized systems. For localized systems which have both localized and extended states, the situation is less clear. Naively, one may expect a similar construction restricted to localized states, but the existence of Griffith regions in

states near mobility edge complicates things, so the development of phenomenology for systems with a mobility edge is still an active research problem.

1.3 Thesis Outline

In this thesis, we look at problems regarding the thermalization of entanglement and many-body localization phase transition.

In Chapter 2, we investigate the thermalization of entanglement near thermal equilibrium. Especially, we focus on two one-dimension spin chain models and contrast the dynamics of entanglement entropy between a robustly non-integrable Hamiltonian model and a Floquet model with no conservation laws and the same average Hamiltonian within one period. It is found that the eigenstates of Floquet model in numerics are less affected by finite size effects in terms of entanglement entropy, and the entanglement relaxes slower to equilibrium under Hamiltonian dynamics. We attribute both to the presence of the energy conservation law, which constrains the structure of eigenstates from Hamiltonian and creates slow diffusive transport of energy imbalances. We also show some preliminary results on attempts to quantify the transport of energy imbalance and the dynamics of entropy starting from different initial states.

In Chapter 3, motivated by the good thermalization of Floquet eigenstates under finite size seen in Chapter 2, we propose a one dimensional Floquet spin model with a tunable disorder strength to analyze the many-body localization phase transition numerically. We demonstrate that our model does exhibit a phase transition and is well thermalized/localized at reasonable sizes. The advantage of using a Floquet model over a Hamiltonian is the suppress of finite size effect in the thermal phase, which is of great importance as the phase transition happens in the thermal side at finite size. We particularly focus on two correlation functions which are hard to

observe clearly in Hamiltonian models until large sizes, and show some preliminary finite size analysis results using these two correlations.

In the last chapter, we attempt to analyze the many-body localization phase transition through a simplified infinite randomness renormalization group approach, which imposes symmetric rules on thermal and localized regions. Because of the simplification, it is possible to obtain the critical point probability distribution and the exponents for the stability of the critical point analytically or up to numeric precision. Particularly, this approach produces a fractal thermal Griffith structure which seems to be a qualitatively correct feature of the transition, and its fractal dimensions can also be found at critical point or "deep" in the thermal phase near the critical point.

Chapter 2

Thermalization of entanglement

2.1 Introduction

Quantum entanglement has recently been a central topic in theoretical physics. Many aspects of the dynamics of entanglement have been recently studied, such as ballistic spreading of the entanglement in integrable [27–29, 39] and nonintegrable [30, 40] systems, logarithmic spreading in many-body localized systems [32, 34], and sub-ballistic spreading due to quantum Griffiths effects [41]. In many of these examples, the entanglement spreads more rapidly than conserved quantities that must be transported by currents.

Much of the previous work on the dynamics of entanglement, however, has emphasized far-from-equilibrium regimes, particularly those following a quantum quench. In this chapter, we instead explore the entanglement dynamics near equilibrium in nonintegrable, thermalizing spin chains [42] of finite length. For example, if we start in a nonentangled initial pure state, the entanglement entropy grows linearly with time at early time due to the "ballistic" spreading of entanglement [30, 40], but then saturates to its "volume-law" equilibrium value at long time. The lower two data sets in Fig. 2.1 illustrate this. As in our introduction in Chapter 1.1.2, in the limit of a long

spin chain, this isolated system is reservoir that thermalizes all of its subsystems, and the extensive part of the final equilibrium value of the entanglement entropy is equal to the thermal equilibrium entropy at the corresponding temperature, which is set by the total energy of the initial state. We call this process, in which the entanglement entropy approaches the thermal equilibrium entropy, the "thermalization of entanglement". Note if we consider the special case in which the initial state is an exact many-body eigenstate, then there is no dynamics and the entanglement entropy is expected to be equal to the thermal entropy at the corresponding energy, according to the eigenstate thermalization hypothesis (ETH) [4, 5, 7] discussed in Chapter 1.1.3.

In this chapter we will focus on the late time, near equilibrium regime of the entanglement dynamics, as well as the spontaneous fluctuations of entanglement in pure states sampled from the equilibrium density operator. Most results in this chapter are presented in 2015 APS March Meeting and reported in the paper [43]. In Section 2.2, we introduce a nonintegrable, quantum-chaotic model Hamiltonian and its corresponding Floquet operator, where the extensive energy conservation is removed. In Section 2.3, we first examine the distribution of entanglement entropy of eigenstates of the Hamiltonian and the Floquet operators, finding that the presence of the conservation law affects the distribution. In Section 2.4, we study the dynamics of entanglement entropy near equilibrium. We study three scenarios: starting from a product state of two random pure states, starting from generalized Bell states with two different pairing schemes, and the autocorrelation of the spontaneous fluctuations of the entanglement entropy. In all cases, we find the Floquet system thermalizes entanglement faster than the Hamiltonian system. In Section 2.5 we attempt to make the relation between the dynamics of entanglement entropy and the transport of energy imbalance more quantitative by investigating many more initial states. We represent the energy imbalance by a square of energy difference between two half chains, and this quantity is found to be strongly correlated with thermalization of

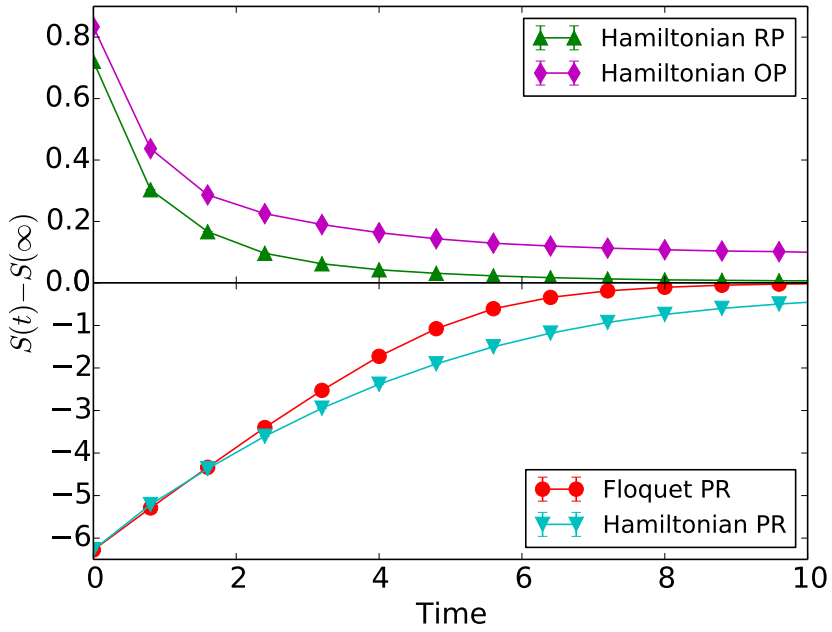

Figure 2.1: Time evolution of the entanglement entropy for $L = 14$ for: product random (PR) initial states under Floquet dynamics (2) with $\tau = 0.8$ (red line with circles) as well as Hamiltonian dynamics (2.1) (blue line with down triangles); "generalized Bell" initial states made from pairs of random pure (RP) states (green line with up triangles) and from "oppositely paired" (OP) states (purple line with diamonds) both under Hamiltonian dynamics. Each case is averaged over 400 initial pure states, and the error estimates are too small to be visible in this figure. See main text for more details.

entropy in many cases, but exceptions do exist. In Section 2.6, we summarize our findings.

2.2 Models

To study a system that is robustly nonintegrable and strongly thermalizing, we choose the spin-1/2 Ising chain with both longitudinal and transverse fields. Its Hamiltonian is

$$H = \sum_{i=1}^{L} g\sigma_i^x + \sum_{i=1}^{L} h\sigma_i^z + \sum_{i=1}^{L-1} J\sigma_i^z\sigma_{i+1}^z \ , \tag{2.1}$$

where σ_i^x and σ_i^z are Pauli matrices at site i. We use open boundary conditions and set the parameters to $(g, h, J) = (0.9045, 0.8090, 1.0)$, for which this model has been shown to be robustly nonintegrable and strongly thermalizing for system sizes readily accessible to exact diagonalization studies [30,44]. Here we avoid the situation where $g = J$ and h is so small that perturbative approach is valid, in which case this model is integrable and has E_8 symmetry [45]. The only conservation laws that this system is known to have at this parameter choice (other than projections on to its exact eigenstates) are total energy, and parity under spatial reflection of the chain ($i \to (L + 1 - i)$). This system's "hydrodynamics" are simply its conserved energy moving diffusively and subject to random local currents due to the system's quantum-chaotic unitary dynamics. We set the Planck constant $\hbar$ to unity so that time and energy have inverse units of each other, and all energies and frequencies are in units of the interaction $J = 1$.

To explore the effects of removing the conservation of total energy, we also study a Floquet system that is a modification of (2.1). We decompose the Hamiltonian into two parts, $H_z = \sum_i (h\sigma_i^z + \sigma_i^z \sigma_{i+1}^z)$ and $H_x = \sum_i g\sigma_i^x$. We periodically drive the system with a time-dependent Hamiltonian that is in turn $H(t) = 2H_z$ for a time interval of $\tau/2$ and then $H(t) = 2H_x$ for the next $\tau/2$, and repeat. The time-averaged Hamiltonian is thus unchanged, but the periodic switching changes the energy conservation from conservation of the extensive total energy to conservation of energy only modulo $(2\pi/\tau)$. This change removes the diffusive transport of energy as a slow "hydrodynamic" mode while otherwise changing the model as little as possible. The Floquet operator that produces the unitary time evolution through one full period is

$$U_F(\tau) = \mathrm{e}^{-iH_x\tau}\mathrm{e}^{-iH_z\tau} \ . \tag{2.2}$$

We choose time step $\tau = 0.8$, which was found in Ref. [44] to produce a rapid relaxation of the total energy within a few time steps. Specifically, this choice is based on the relaxation of the total energy under different choices of τ for $L = 12$, as is shown in Fig. 2.2, which demonstrates how the autocorrelation of the total energy decays under discrete Floquet dynamics: $\mathrm{Tr}\{HU_F^\dagger(n\tau)HU_F(n\tau)\}$. Both $\tau = 0.8$ and $\tau = 1$ relax the total energy very quickly so that the system approaches equilibrium within of order one time step, while for $\tau = 0.6$ the energy relaxation has a much slower component. $\tau = 1$ leads to a more oscillatory behavior compared with $\tau = 0.8$. Therefore $\tau = 0.8$ emerges as a nice choice for our studies. The eigenvalues of $U_F(\tau)$ are complex numbers of magnitude one. Note that time is in a certain sense discrete (integer multiples of τ) for this Floquet system. The Hamiltonian system, with conserved total energy, is effectively the case $\tau = 0$, which we contrast here with the Floquet system with $\tau = 0.8$ where the total energy is not conserved and relaxes very quickly. Of course, there is an interesting crossover between these two limits [1], but we do not explore that crossover here.

Throughout this chapter, we consider the bipartite entanglement entropy of pure states, quantified by the von Neumann entropy of the reduced density operator of a half chain: $S = -\mathrm{Tr}\{\rho_L \log_2 \rho_L\} = -\mathrm{Tr}\{\rho_R \log_2 \rho_R\}$. We study chains of even length, and ρ_L and ρ_R are the reduced density operators of the left and right half chains, respectively. Note that we measure the entropy in bits.

2.3 Entanglement entropies of eigenstates

We first look at the entanglement entropy of the eigenstates of the Hamiltonian (2.1) and of the Floquet operator (2.2), compared to random pure states of the full chain. Figure 2.3 shows the distributions of these entanglement entropies for $L = 16$.

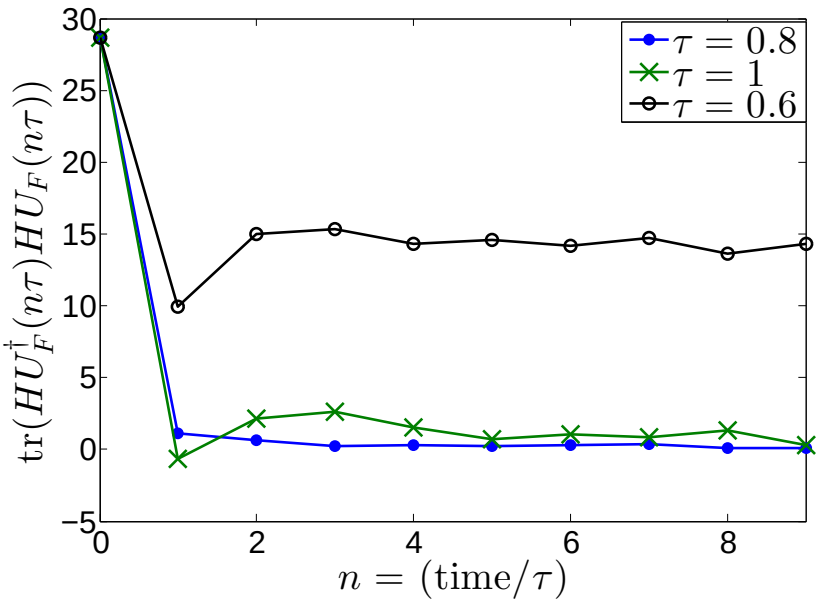

Figure 2.2: Relaxation of total energy under Floquet dynamics for $L = 12$ with different choices of driving period τ.

We can see that the entanglement of the eigenstates of the Floquet operator is close to that of random pure states, first derived by Page [46]:

$$S^R(L) = \frac{L}{2} - \frac{1}{2\ln 2} - \mathcal{O}\left(\frac{1}{2^L}\right) . \tag{2.3}$$

This is consistent with previous studies which have shown that a Floquet dynamics thermalizes a subsystem to infinite temperature [1, 44, 47, 48]. The eigenstates of the Hamiltonian, on the other hand, all have entanglement entropies that are a fraction of a bit or more less than random pure states. What is the source of this difference? It is because the Hamiltonian eigenstates are eigenstates of the extensive conserved total energy, while the random pure states and the Floquet eigenstates are not constrained by an extensive conserved quantity. This causes the probability distribution of the

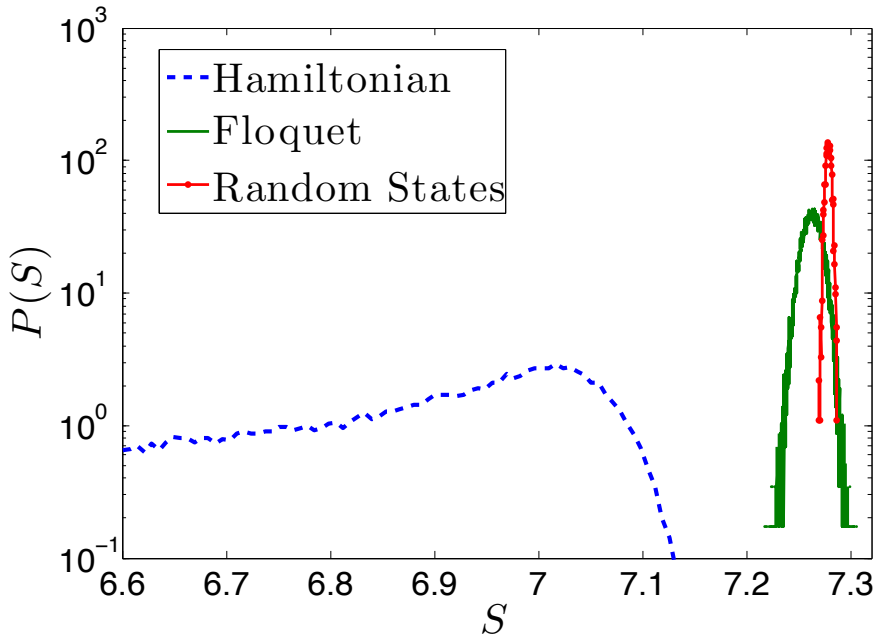

Figure 2.3: Normalized histogram of the entanglement entropy for $L = 16$ for: (dashed blue line) the eigenstates of the Hamiltonian (2.1); the eigenstates of the Floquet operator (2.2) with $\tau = 0.8$ (solid green line); and for random pure states of the full chain (very narrow red distribution), where the histogram is over 2000 randomly generated pure states.

energy of a half chain to be narrower for the Hamiltonian system, since if one half chain has a high energy (compared to its share of the eigenenergy) then the other half chain has to have an energy that is low by the same amount. This suppresses the volume of the possible space of half-chain states whose energy is either high or low, resulting in a reduced entropy of the half-chain and thus reduced entanglement entropy, even for the Hamiltonian eigenstates at energies that correspond to infinite temperature. This goes along with the recent observation that the finite-size deviations of the eigenstates of the Hamiltonian from the Eigenstate Thermalization Hypothesis are larger than those of the eigenstates of the Floquet operator [44]: energy conservation somewhat impedes thermalization.

2.4 Dynamics of Entanglement near equilibrium

Now we turn to the dynamics of the entanglement entropy. The dynamics of a linear operator is set by the matrix elements of the operator between energy eigenstates (or eigenstates of the Floquet operator) and the eigenenergies. But the entanglement is not a linear operator, so its dynamics cannot be determined so simply. We explore the near-equilibrium dynamics of the entanglement in two different ways. First we study the relaxation of the entanglement to its equilibrium value from particular initial states with either low or high entanglement. We then explore the dynamics of the spontaneous fluctuations of the entanglement entropy during the unitary time evolution of a random pure state of the full spin chain. From these studies we can clearly show that the entanglement dynamics is slower for the Hamiltonian system, since some of the entanglement entropy is connected to the slow diffusion of energy between the two half-chains. In the Floquet system, on the other hand, near equilibrium the entanglement relaxes to equilibrium with a simple-exponential behavior in time, with a relaxation time that is apparently independent of the system size.

2.4.1 Product of Random Pure states

For initial states with zero entanglement between the two half chains, we use a product of random (PR in Fig. 2.1) half-chain pure states $|\psi(t = 0)\rangle = |\psi_L\rangle \otimes |\psi_R\rangle$, where $|\psi_L\rangle$ and $|\psi_R\rangle$ are picked from the ensemble of random pure states of the left and the right half chain, respectively. On average these states have energy close to 0, so the system is near infinite temperature and starts with zero entanglement entropy. As random pure states are chosen for the half chains, the expected energy distribution between left and right halves is close to the equilibrium distribution (at infinite temperature), indicating only a small energy transport between two halves is required for thermalization. Fig. 2.1 plots the time-dependent entanglement entropy

under Hamiltonian and Floquet dynamics for $L = 14$. The long-time average $S(\infty)$ is estimated by averaging $S(t)$ from $t = 2500\tau$ to $t = 2999\tau$.

It is clear from Fig. 2.1 that the Floquet system has faster relaxation of the entanglement entropy towards its saturation value at long times, even though the initial spreading rate of the entanglement is the same for these two systems. Since the only significant difference between these two unitary dynamics is whether or not energy conservation and thus energy transport is present, Fig. 2.1 suggests that the slow dynamical modes of this system associated with energy transport do also slow down the long-time thermalization of the entanglement.

2.4.2 Generalized Bell States

To explore the thermalization of the entanglement from initial states with *higher* entanglement than equilibrium, we use initial states that maximize the entanglement entropy; we call these "generalized Bell states". These states have Schmidt decomposition

$$|\psi_B\rangle = \frac{1}{\sqrt{2^{L/2}}} \sum_{i=1}^{2^{L/2}} |L_i\rangle \otimes |R_i\rangle \ , \tag{2.4}$$

where the sets $\{|L_i\rangle\}$ and $\{|R_i\rangle\}$ are respectively complete orthonormal bases for left and right half chains. Since these initial states have higher entanglement entropy than equilibrium, their entropy *decreases* as it thermalizes. This is an amusing apparent "violation" of the second law of thermodynamics, but it is actually not thermodynamics, since the decrease is by less than one bit (very close to $1/(2\ln 2)$ by Eq. (2.3)), and thus far from extensive.

The random pure (RP) Bell states are made by independently choosing a random orthonormal basis for each half-chain. To make initial Bell states that also have very large energy differences between the two half-chains, we make the opposite paired

(OP) states that can be written as

$$|\psi(t=0)\rangle = \frac{1}{\sqrt{2^{L/2}}} \sum_{i=1}^{2^{L/2}} \mathrm{e}^{i\theta_i} |E_i^h\rangle_{left} \otimes |E_{2^{L/2}+1-i}^h\rangle_{right} \ , \tag{2.5}$$

where the $|E_i^h\rangle$ are the eigenstates of the half-chain Hamiltonian (Hamiltonian (2.1) with $L/2$ sites), with their eigenenergies ordered according to $E_i^h \leq E_{i+1}^h$. Therefore, by construction, many Schmidt pairs in these opposite paired Bell states have large energy imbalance between the two half-chains, unlike the random pure Bell states where the energy imbalance between the two halves is small. The contrast between them shows how the slow diffusive relaxation of the energy imbalance affects entanglement thermalization. The ensemble of OP states that we average over is obtained by choosing random phases $\{\theta_i\}$.

The time evolution of the entanglement entropy for a $L = 14$ spin chain starting from generalized Bell states of pairs of random pure (RP) states as well as generalized Bell states with opposite pairing (OP) under Hamiltonian dynamics are shown in Fig. 2.1, with the estimated long time average subtracted. For the opposite paired (OP) initial states, the initial large energy differences between the two half-chains in many of the Schmidt pairs make the excess entanglement long-lived, since the relaxation of these energy differences requires diffusion of the energy over the full length of the chain. For the RP initial states, on the other hand, the half-chain states are random so do not show nonequilibrium energy correlations, and the excess entanglement relaxes to equilibrium much more rapidly than it does for the OP states. This observation hence provides additional evidence of the coupling between entanglement entropy relaxation and energy transport under Hamiltonian dynamics.

Fig. 2.4 gives a more detailed view of the thermalization of the excess entanglement entropy starting from these generalized Bell initial states. Here RP initial states under Floquet dynamics are also shown; since the Floquet system does not have

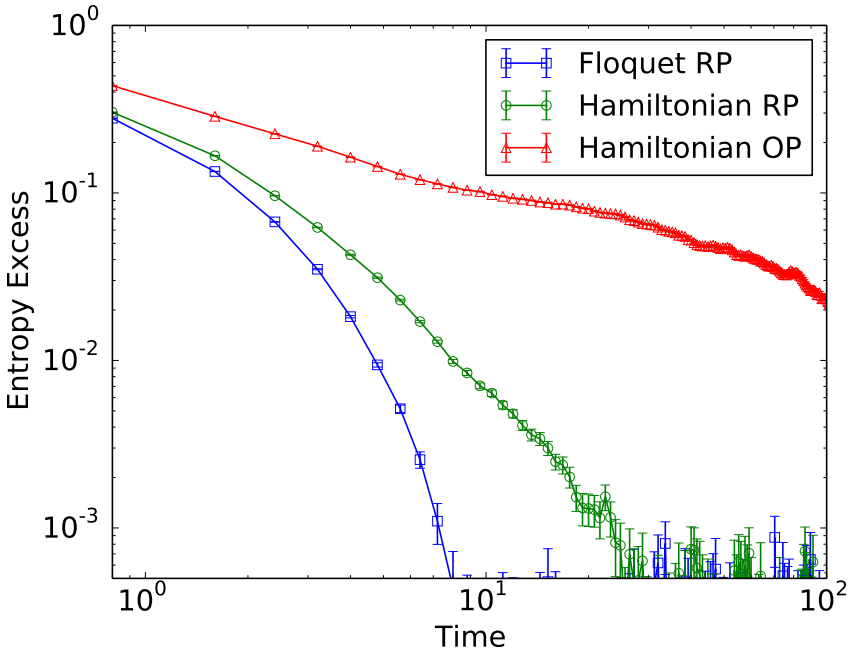

Figure 2.4: Thermalization of entanglement entropy in three cases for $L = 14$ (log-log scale): from random pure (RP) generalized Bell states under Hamiltonian dynamics (circular markers, green); from RP generalized Bell states under Floquet dynamics (square markers, blue); and from oppositely paired (OP) generalized Bell states under Hamiltonian dynamics (triangular markers, red). Within Hamiltonian dynamics, the larger initial energy imbalance for the OP initial states dictates a slower thermalization of the entanglement, while the absence of energy conservation for the Floquet system allows the fastest thermalization of entanglement entropy among all cases considered. See main text for description of initial states.

conserved energy we cannot construct an OP initial state for it. This figure again shows the clear importance of energy transport for entanglement thermalization. The excess entropy of the RP initial states decays away faster for the Floquet system as compared to the Hamiltonian system, since the thermalization of the Floquet system is not constrained by an extensive conserved energy. The strong initial anticorrelation between the energies of the two half-chains greatly slows down the thermalization of the entanglement for the OP initial states under Hamiltonian dynamics.

2.4.3 Autocorrelation of entanglement

Next we examine the dynamics of the spontaneous fluctuations of the entanglement entropy at equilibrium at infinite temperature, where all pure states are equally likely. Therefore, we simply pick many random pure states of the full chain and calculate the unitary time evolution of each initial state over many time steps. We measure the autocorrelation of the entropy for each realization (indexed by i) as

$$R_i(t) = \frac{1}{M}\sum_{m=1}^{M}\left[S_i(t_m) - \bar{S}_i\right]\left[S_i(t_m + t) - \bar{S}_i\right] \ , \tag{2.6}$$

where each run has in total 30000 time points t_m, equally spaced in time by Δt, and $S_i(t)$ is the entropy at time t. Thus we measure the autocorrelation at integer multiples of the time step: $t = n\Delta t$. M is the maximum number of pairs that can be extracted from the time series. Each random initial state gives slightly different time-averaged entropies $\bar{S}_i$, and thus for each run we subtract its average in Eq. (2.6). Then we average over runs and normalize the autocorrelation to be one at time difference $t = 0$. The statistical errors are estimated from this averaging over runs.

Fig. 2.5 plots the autocorrelation under Hamiltonian and Floquet dynamics with systems of different sizes: $L = 10$, $L = 12$ and $L = 14$. For $L = 10$ the number of independent runs in each case is $N = 400$, while for $L = 12$ and $L = 14$ we chose $N = 100$. With $\tau = 0.8$ as before, our time points are spaced by $\Delta t = 3\tau$ for Hamiltonian dynamics and $\Delta t = 2\tau$ for Floquet dynamics. It can be easily seen from Fig. 2.5 that the relaxation of autocorrelations under Floquet dynamics is systematically faster. Particularly, the autocorrelation in the Floquet system assumes a simple exponential decay. This observation indicates that under the Floquet dynamics a random state "relaxes" to equilibrium by independent and unconstrained local relaxation. In the Hamiltonian system, on the other hand, a spontaneous fluctuation that rearranges the energy density on a long length scale is necessarily slow, due to the slow energy

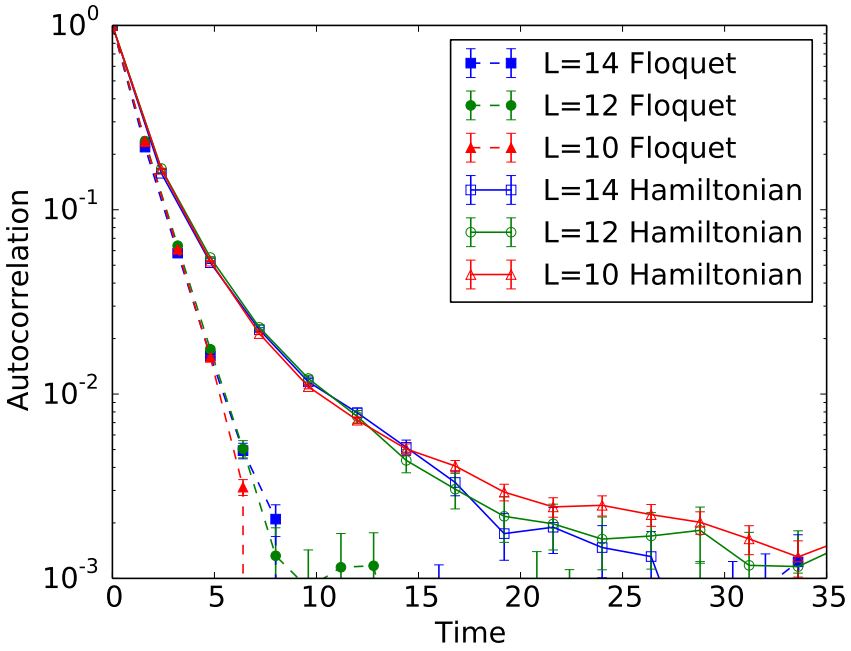

Figure 2.5: Autocorrelation of the entanglement entropy vs. time for random pure states under Hamiltonian (solid lines) as well as Floquet dynamics (dashed lines) with different system sizes L in log-linear scale. For each case, the autocorrelation is normalized to be one at time zero. Under Floquet dynamics, the autocorrelation decays as a simple exponential function of time, and faster than under Hamiltonian dynamics. Only weak size dependence of this normalized autocorrelation is observed under either dynamics.

diffusion. Thus any influence of such fluctuations on the entanglement must relax slowly. Clearly we are seeing such an influence that is causing the slower long-time relaxation of the entanglement autocorrelation in the Hamiltonian system. Fig. 2.6 suggests that the autocorrelation under Hamiltonian dynamics decays exponentially in square root of time, as curves become roughly straight when plotted against $\sqrt{t}$ in a semi-log plot, and the straightness increases as system size increases. This scaling may be understood as fluctuation of entanglement entropy coupled to operators on the spin chain. At time t the fluctuation couples to the $O(4^l)$ operators on a size of $l \sim \sqrt{t}$ by diffusion, of which only $O(1)$ operators are slow, so only $O(1/4^l) \sim \exp(-c\sqrt{t})$ fraction of the information about the initial fluctuation is left at time t, where c is some constant, resulting in an exponential decay of autocorrelation in $\sqrt{t}$. The same

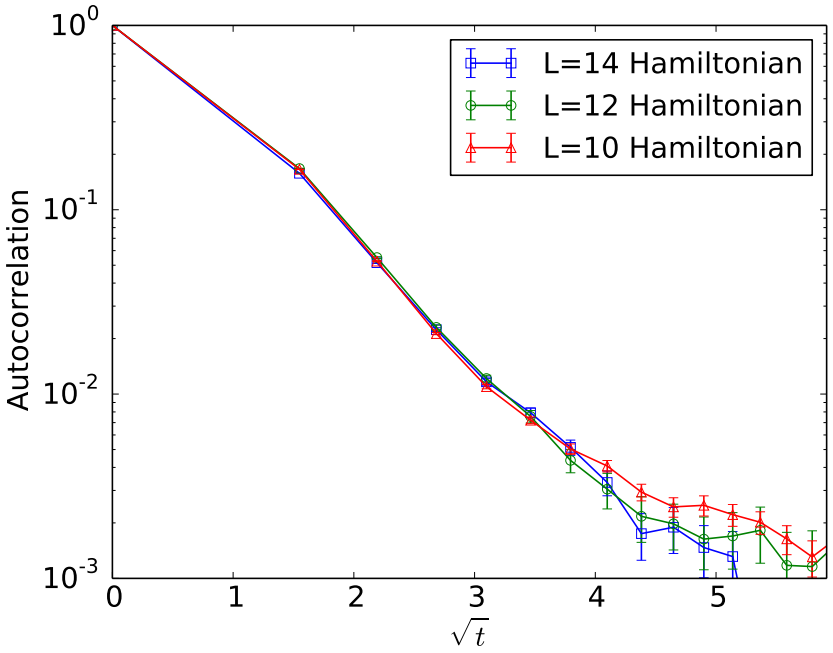

Figure 2.6: Autocorrelation of the entanglement entropy under Hamiltonian dynamics vs. square root of time for random pure states with different system sizes L. On this semi-log scale, all three curves roughly follow a straight line and the tail becomes more straight as system size increases.

reasoning may also be applied to the Floquet system, where the slowest modes instead have [49] $l \sim t$, thus leading to a the observed simple exponential decay as is shown in Figure 2.5.

One may also note here that under either dynamics, the relaxation of these autocorrelations has little dependence on system size. This indicates that the fluctuations that are contributing here are on length scales smaller than the $L = 10$ systems. For the Floquet system this is consistent with the relaxation being simply local, so any longer length scale slow operators [49] apparently do not couple substantially to the entanglement fluctuations. For the Hamiltonian systems this absence of size dependence suggests that over the time range probed here, the energy fluctuations that couple to the entanglement are on length scales smaller than the length of the smaller $L = 10$ system. But the substantially slower relaxation as compared to the Floquet

system suggests that energy transport over a few lattice spacings does couple to the entanglement fluctuations.

2.5 Energy Imbalance and Relaxation of Entropy

In the above we have seen that diffusive relaxation of the energy distribution slows down the thermalization of entanglement entropy near equilibrium. A natural follow-up analysis would then be to investigate any quantitative relation between energy imbalance and the relaxation of entanglement entropy in the Hamiltonian. In this section, we show some preliminary work in this direction. For simplicity, we represent the energy imbalance as square of energy difference between two half chains: $\delta E^2(t) = \langle (H_L - H_R)^2 \rangle(t)$. This can be thought of as the energy imbalance mode with the longest wavelength inside the chain, and in general it should be the most relevant near equilibrium because imbalance in shorter wavelength is expected to be transported away faster. To get a more complete picture, in the following we consider more initial states and here is the definition of states shown in Fig. 2.7:

- *Small Bell 16*: A modification of OP states which can have initial entanglement entropy below the thermal value. As in Eq. (2.5), we consider a list of left half chain eigenstates $|E_1^h\rangle_{left}, |E_2^h\rangle_{left}, \cdots, |E_N^h\rangle_{left}$ and right half chain eigenstates $|E_N^h\rangle_{right}, |E_{N-1}^h\rangle_{right}, \cdots, |E_1^h\rangle_{right}$ which are in opposite energy orderings of each other, where $E_i^h \leq E_{i+1}^h$ and $N = 2^{L/2}$ is the dimension of the half chain Hilbert space. The two lists are divided into M intervals so that each interval has the same number d half chain eigenstates. This requires $M = 2^m$ for some integer $m \leq L/2$. For each interval i, we can construct two random pure states $|\psi_L\rangle_i$ and $|\psi_R\rangle_i$ on the subspace spanned by $|E_{nd+1}^h\rangle_{left}, |E_{nd+2}^h\rangle_{left}, \cdots, |E_{(n+1)d}^h\rangle_{left}$ for the left half chain and $|E_{N-nd}^h\rangle_{right}, |E_{N-nd-1}^h\rangle_{right}, \cdots, |E_{N-(n+1)d+1}^h\rangle_{right}$ for

the right half chain, respectively. Our initial state in this case is then

$$|\psi(t=0)\rangle = \frac{1}{\sqrt{M}} \sum_{i=1}^{M} \mathrm{e}^{i\theta_i} |\psi_L\rangle_i \otimes |\psi_R\rangle_i \tag{2.7}$$

with random phases $\{\theta_i\}$. In the following we choose the state with $M = 16$ intervals; thus comes the number 16 in the name. This initial state has 4 bits of entropy.

- *One Side Energy 14* and *Two Side Energy 14*: A further modification of Small Bell states defined above. We again start with a list of left half chain eigenstates $|E_1^h\rangle_{left}, |E_2^h\rangle_{left}, \cdots, |E_N^h\rangle_{left}$ and right half chain eigenstates $|E_N^h\rangle_{right}, |E_{N-1}^h\rangle_{right}, \cdots, |E_1^h\rangle_{right}$ in opposite ordering of energies, but instead of dividing them into M intervals all having d states, we divide the lists into interval of equal energy differences. More precisely, we divide the half chain energy spectrum into M intervals each with energy difference $\Delta E = (E_N^h - E_i^h)/M$, and label the end points of intervals as $e_1 = E_1^h, e_2 = e_1 + \Delta E, \cdots, e_{M+1} = E_N^h$. Because of numeric precision, the probability of any half chain eigenstate having energy exactly equal to e_i for $i \neq 1$, $M+1$ is 0. In the "one side" case, we only apply this division to left half chain eigenstates, so that each $|E_i\rangle_{left}$ goes into interval j if $e_j \leq E_i^h \leq e_{j+1}$. Under this assignment, some energy intervals may actually be empty if no $|E_i^h\rangle_{left}$ falls into it, and for simplicity we will re-label all non-empty intervals consecutively from 1 to $M' \leq M$. For right half chain eigenstates, we still divide them into M' intervals and $|E_i^h\rangle_{right}$ would go to interval j if its corresponding left half chain eigenstate $|E_{N-i+1}^h\rangle_{left}$ goes to the jth interval in left list. In the "two side" case on the other hand, we also divide the spectrum of right half chain into M intervals and put eigenstates into these intervals as for left half chain. As a result, the ith interval from the left half chain contains identical half chain eigenstates as in the $(M+1-i)$th interval

from the right half chain (empty intervals included). As in the "one side" case, we can relabel intervals from both half chains to exclude empty intervals so that there will be $M^{'} \leq M$ non-empty intervals from either side. We can then construct random pure states $|\psi_L\rangle_i$ and $|\psi_R\rangle_i$ from subspaces spanned by half chain eigenstates from the ith (non-empty) interval of left and right half chains respectively, The initial state is then

$$|\psi(t=0)\rangle = \frac{1}{Z}\sum_{i=1}^{M^{'}} \sqrt[4]{n_L^i n_R^i}\mathrm{e}^{i\theta_i}|\psi_L\rangle_i \otimes |\psi_R\rangle_i \tag{2.8}$$

with random phases $\{\theta_i\}$, where n_L^i and n_R^i are the dimensions of the subspaces from the ith left and right half chain intervals, and Z is a normalization constant. The amplitudes are chosen to ensure a "fair" mix of states in this generalized Bell state. Particularly, in the "one side" case, for any i we have $n_L^i = n_R^i$ so that $\sqrt[4]{n_L^i n_R^i}/Z = \sqrt{n_L^i/N}$, thus it weighs each product state $|\psi_L\rangle_i \otimes |\psi_R\rangle_i$ according to the number of orthonormal states used to construct each random pure state. The 14 here means $M^{'} = 14$. Moreover, if $M^{'} = 1$ we get back to a PR state, and when $M^{'} = N$, we obtain an OP state.

- *Restricted product random states*: Initial state is a product state of two random pure states formed on a restricted subspace of half-chain eigenstates:

$$|\psi(t=0)\rangle = |\psi_L\rangle \otimes |\psi_R\rangle\,. \tag{2.9}$$

  Here $|\psi\rangle_L$ and $|\psi\rangle_R$ are random pure states constructed on the subspace spanned by the 12 half chain eigenstates $\{|E_i^h\rangle\}$ with smallest energy magnitude $|E_i^h|$.

- *Restricted product random 57 states*: A restricted product random state as above, where $|\psi\rangle_L$ and $|\psi\rangle_R$ are constructed on the subspace spanned by the 57 half chain eigenstates with smallest energy magnitude instead 12. We choose 57

because this state appears to relax fastest among all restricted product random states using different number of half-chain eigenstates.

- *Restricted opposite pairing states*: An OP state where the first 12 half-chain eigenstates with smallest energy magnitude are chosen to pair oppositely in energy in Eq. (2.5). This state would be qualitatively similar to the original OP state but with smaller entanglement entropy.

- *Restricted random pure paired states*: An RP state, where the half-chain orthonormal basis of random pure states in Eq. (2.4) come from the subspace spanned by the first 12 half-chain eigenstates with smallest energy magnitude. It has smaller entanglement entropy compared to the original RP state.

- *Random product states*: A product state of random spins at each site:

$$|\psi(t=0)\rangle = |\vec{s}_1\rangle \otimes |\vec{s}_2\rangle \otimes \cdots \otimes |\vec{s}_L\rangle \tag{2.10}$$

with

$$|\vec{s}_i\rangle = \cos\left(\frac{\theta_i}{2}\right) |\uparrow_i\rangle + \mathrm{e}^{i\phi_i} \sin\left(\frac{\theta_i}{2}\right) |\downarrow_i\rangle \tag{2.11}$$

where random phases $\theta_i \in [0, \pi)$ and $\phi_i \in [0, 2\pi)$.

- *Random pair states with different angles*: A generalization of OP states, which are still generalized bell states from pairing half-chain eigenstates:

$$|\psi(t=0)\rangle = \frac{1}{2^{L/2}} \sum_{i=1}^{2^{L/2}} \mathrm{e}^{i\theta_i} |E_i^h\rangle_{left} \otimes |E_{f(i)}^h\rangle_{right} \tag{2.12}$$

with $E_i^h \leq E_{i+1}^h$ and $\tilde{E}_{f(i)}^h \leq \tilde{E}_{f(i+1)}^h$, where the "effective" energy is defined as

$$\tilde{E}_i^h = E_i^h \sin(\alpha) + G_i \cos(\alpha) \tag{2.13}$$

Here $\{G_i\}$ is a set of independent Gaussian random variables with mean 0 and standard deviation equal to the sample standard deviation of $\{E_i^h\}$. α is the angle quoted in the legend of Fig. 2.7. When $\alpha = -\pi/2$, we recover the OP states, and when $\alpha = 0$ half-chain eigenstates are paired randomly.

Fig. 2.7 shows the entropy difference $\Delta S(t) = S(t) - S(\infty)$ versus δE^2 as various states approach equilibrium for Hamiltonian system with $L = 12$, where $S(\infty)$ is estimated from long time averages. Long time averages of energy imbalance δE^2 are also subtracted in the plots. Results are binned together according to time and each bin is of 30 time units wide. Error bars represent the standard errors within each bin when averaged over 400 runs. The product random states are PR states described in Sec. 2.4.1, and as expected for them δE^2 is at equilibrium value almost from the beginning.

It can be seen that when states are approaching equilibrium, most of them roughly fall on a line, suggesting a linear relation between ΔS and δE^2. This provides a more quantitative description of our observation in Sec. 2.4.2 that larger energy imbalance results in slower entropy relaxation. One would also expect this linear coefficient to be almost independent of initial conditions when we are this close to thermal equilibrium, though a closer look around 0 given in Fig. 2.7(b) suggests multiple slopes when approaching equilibrium. This seeming surprise, however, may merely come from finite size effects, as it actually has been observed (not shown here) that with $L = 12$ states starting with $\Delta S > 0$ may reach a slightly different equilibrium condition that those starting with $\Delta S < 0$, and these differences may translate into slightly different linear coefficients between ΔS and δE^2. On the other hand, it is interesting to note that there are initial states like random product states which do not develop a linear relation between ΔS and δE^2 on the scale plotted and seems to deviate from our expectation that larger energy imbalance impedes entropy relaxation more. For instance, random product states and the full product random states have entropy

relax slower than that of the restricted random product states using 57 eigenstates, even though the former two both have smaller δE^2 to start with. One possible explanation may be related to how we characterize the energy imbalance here, since the exceptional states in our case all have δE^2 close to their equilibrium values. Because δE^2 only represent the the longest wavelength energy imbalance mode, as they become unusually small, modes of shorter wavelength would start to have significant influence on energy transport even at late stages of thermalization, and their relations with thermalization of entanglement are not correctly captured in Fig. 2.7. Therefore, a more thorough study of the relation between energy imbalance transport and entanglement entropy relaxation in Hamiltonian systems can be a possible future project which may provide further insight into the details of thermalization of entanglement.

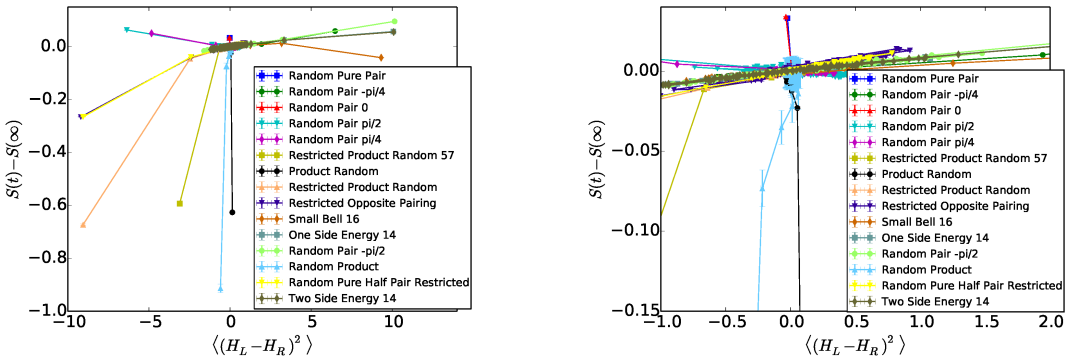

(a) (b)

Figure 2.7: Entropy difference against energy imbalance (long time averages subtracted) with various initial states along the evolution. All data are grouped in bins of 30 time units wide. Most states roughly fall on a line when approaching equilibrium but exceptions do exist. (b) gives a closer look at the center and multiple slopes can be observed which may result from finite size effect.

2.6 Conclusion

In conclusion, we have investigated the thermalization of the entanglement entropy by comparing state evolution of spin chains under Hamiltonian dynamics and Flo-

quet dynamics, with the two systems having the same time-averaged Hamiltonian. Eigenstates of these two dynamics have quite different distributions of the entanglement entropy. The Floquet eigenstates all have entanglement close to that of random pure states, while the Hamiltonian eigenstates all have significantly less entanglement due to the constraint of total energy conservation. We show that the entanglement entropy relaxes to equilibrium more slowly under Hamiltonian dynamics, both for initial states well away from equilibrium and for the spontaneous fluctuations of the entanglement entropy at equilibrium. The Hamiltonian system has slow diffusive energy transport, while the Floquet system does not. This slow diffusive relaxation of the energy distribution in the Hamiltonian system results in slow relaxation near equilibrium of the entanglement entropy. We further demonstrate some preliminary investigation of the relation between energy imbalance and entropy relaxation. Characterizing energy imbalance by its longest wavelength mode, we find most initial states follow our expectation that a larger energy imbalance leads to slower relaxation of entanglement entropy. However, exceptions do exist which confine the validity of our simple picture and requires further more thorough study of the topic.

Chapter 3

Floquet model of the many-body localization transition

3.1 Introduction

In the last chapter we have seen that conservation laws may impede the thermalization of entanglement entropy, and that at finite sizes Floquet systems' eigenstates are better thermalized than those from Hamiltonian systems. In this chapter, with the help of these observations, we will now turn to the study of a particular phase transition: the dynamical quantum phase transition between many-body localization (MBL) and thermalization. This phase transition has attracted much recent interest, but remains poorly understood [2, 13, 25, 26, 41, 50–65]. It is a new type of phase transition for which we have not (yet?) found methods that allow a detailed and convincing study of its properties. Much of the work studying this phase transition is numerical, using various numerical approaches, particularly for one-dimensional spin chain models. Such studies have a large amount of freedom in choosing the specific model to focus on, since all one really needs is a model exhibiting the MBL phase, the thermal phase, and the phase transition between them. In this chapter we want

address the question of what features one should possibly look for in choosing the "best" type of model to study.

The many-body localized phase is now understood to be a new type of integrable system, with an extensive number of localized conserved quantities [38, 66]. The phase transition into the MBL phase from the thermal phase can thus be thought of as the emergence of all these new conservation laws. This suggests that an important property of the thermal phase may be its lack of localized conserved quantities. In finite sized systems any conserved quantity is in some sense localized due to the finite size, so one can thus argue that the best representative of the thermal phase may be a phase with zero local conservation laws, not even energy. Such models are available in the form of so-called Floquet models [47, 48, 67] which are also explored in Chapter 2. They have a discrete time dynamics where the time evolution operator that advances time by one unit of time is a local unitary operator, U. Generically, such Floquet models have no local conservation laws or symmetries in their thermal phase, and when they thermalize they maximize the entropy without any constraint, so in a certain sense they thermalize to infinite temperature. As shown in Chapter 2, having no conservation laws allows such Floquet models to thermalize faster than the corresponding Hamiltonian models that have conserved energy slowing down their thermalization [43].

In this chapter, we propose a specific such spin-1/2-chain Floquet model with no conservation laws. In the limit of zero disorder this model becomes the model introduced in Chapter 2 as an example of a Floquet model that thermalizes very rapidly [43, 49]. We will show results of several quantities for this model which are frequently used to characterize the transition, and demonstrate that the model can indeed reach a fully thermalized phase as well as a fully localized phase, and the signal-to-noise ratio is already very good in the thermal regimes at a reasonable system size. Particularly, we will look at two spin correlation functions across the whole

chain. Correlation functions play an important role in studying the "traditional" phase transition, but are under-presented in numerical studies of MBL phase transitions, possibly because of the large noise background appearing in finite size studies, especially on the thermal side, which is exactly the problem that we hope our model can ameliorate.

The model is introduced in Section 3.2. We then discuss our numerical results charactering the transition in Section 3.3. Preliminary finite size analysis using correlation functions is demonstrated in Section 3.4 and we summarize this chapter in Section 3.5.

3.2 Model

The simplest nearest-neighbor interaction in a spin-1/2 chain is an Ising interaction $\sigma_j^z \sigma_{j+1}^z$. So we choose a model that has only this interaction. To make the system nonintegrable and rapidly thermalizing when we are deep in the thermal phase we need to have both a transverse and a longitudinal field. We choose to put the disorder only in the longitudinal field, so the deeply localized limit is quite simple. As we turn on this random longitudinal field, we decrease the (nonrandom) transverse field to keep the mean-square field constant. Thus we arrive at the following unitary time evolution operator:

$$U = \mathrm{e}^{-i\frac{\tau}{2}\sum_{j=1}^{L} gW\sigma_j^x}\, \mathrm{e}^{-i\tau\sum_{j=1}^{L-1}\sigma_j^z\sigma_{j+1}^z - i\tau\sum_{j=1}^{L}(h+g\sqrt{1-W^2}G_j)\sigma_j^z}\, \mathrm{e}^{-i\frac{\tau}{2}\sum_{j=1}^{L} gW\sigma_j^x}\,, \tag{3.1}$$

with open boundary conditions and fixed parameters $(g, h, \tau) = (0.9045, 0.8090, 0.8)$, following Refs. [43, 44]. $\{G_j\}_{j=1}^{L}$ is a set of independent Gaussian standard normal random variables, and σ_i^x and σ_i^z are the Pauli matrices at site i. The model can be

thought of as driving the system periodically with period 2τ with

$$H_x = \sum_{j=1}^{L} gW\sigma_j^x \tag{3.2}$$

$$H_z = \sum_{j=1}^{L-1} \sigma_j^z\sigma_{j+1}^z + \sum_{j=1}^{L}(h + g\sqrt{1-W^2}G_j)\sigma_j^z \tag{3.3}$$

such that H_x acts for a time interval of length τ and H_z then acts for another τ, then it repeats. For convenience we choose here our reference time point at the "center" of H_x's turn, so that U has time reversal symmetry, which makes all eigenvectors real in the basis of products of spins pointing along z directions, making numerical diagonalization of U more efficient. W here controls the disorder strength by scaling the Gaussian random longitudinal fields and the strength of the transverse field. As $W \to 1$, the model becomes the nonrandom Floquet model used in Refs. [43, 44], so it is thermalizes rapidly with only weak finite size effects. As $W \to 0$, the transverse field is turned off and the model is trivially localized with its conserved operators (its "l-bits" [38]) being simply the $\{\sigma_i^z\}$. Tuning W between 0 and 1 thus gives us the dynamical phase transition between the MBL phase and the thermal phase.

3.3 Numerical results

In the following, we investigate several quantities near the MBL phase transition using this Floquet model and exact diagonalization, demonstrating its ability to give reasonably sharp results even for relatively small system sizes.

3.3.1 Entanglement entropy

One quantity that characterizes the phase transition is the entanglement entropy of the eigenstates of the Floquet time evolution operator U. As in Chapter 2, we consider the bipartite entanglement entropy S_E in bits given by the von Neumann

entropy of the reduced density operator of a half chain: $S_E = -\mathrm{Tr}\{\rho_L \log_2 \rho_L\} = -\mathrm{Tr}\{\rho_R \log_2 \rho_R\}$, where ρ_L and ρ_R are the reduced density operators of the left and right half chains when the full chain is in an eigenstate of U and the length L of the chain is an even number. When $W \to 1$, Floquet dynamics thermalizes these half chains to infinite temperature [1, 44, 47, 48, 67], so for large enough L all eigenstates have entanglement entropy close to that of random pure states [43] as is seen in Chapter 2. A random pure state has "volume-law" entanglement entropy [46] as given in Eq. (2.3):

$$S_R(L) = \frac{L}{2} - \frac{1}{2\ln 2} - \mathcal{O}\left(\frac{1}{2^L}\right) , \tag{3.4}$$

and we will normalize our eigenstate entanglement entropies by this value. On the other hand, in the localized phase, eigenstates of U have "boundary-law" entanglement entropy [2,68], so $S_E/S_R \to 0$ as $L \to \infty$ in the MBL phase. Fig. 3.1 shows the normalized mean entanglement entropy $S_{norm} = \langle \overline{S}_E \rangle / S_R$ across the transition as W and L are varied. Here $\overline{\cdots}$ indicates averaging over all eigenstates for one disorder realization, and $\langle \cdots \rangle$ indicates averaging over different realizations of the disorder. There are 100 disorder realizations up to size 10 and 50 realizations for size 12. We can see the transition of this normalized entropy from 0 (localized) to 1 (thermal) as W increases, with the transition becoming a steeper function of W as L is increased, as expected and as seen in Hamiltonian models [51, 57].

Another quantity related to entanglement entropy that is studied [51, 57] is the variance of the distribution of S_E. Our variance is calculated as $\sigma_E^2 = \langle \overline{(S_E - S_{ave})^2} \rangle$, where S_{ave} is the average entanglement entropy over all eigenstates from all realizations of the disorder. The results are shown in Fig. 3.2, which shows the peak in this quantity that increases strongly with L and occurs on the thermal side of the phase transition; the location of the peak approaches the transition as L is increased [51,57]. This entanglement variance is expected to vanish in the limit of large L in the thermal

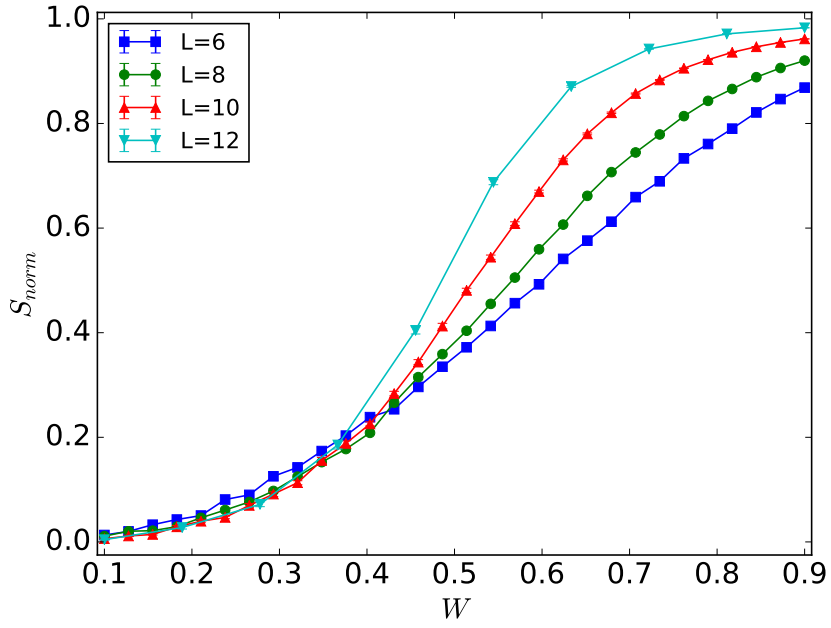

Figure 3.1: The normalized average entanglement entropy of all eigenstates. The normalization is chosen so a random pure state has normalized entropy one. The statistical error bars where not visible are smaller than the symbols. Our estimate of the critical point from other data, shown below, is $W_c \simeq 0.3$, with the MBL phase at $W < W_c$ and the thermal phase at $W > W_c$.

phase, as entropies of all eigenstates approach the Page value [43] S_R. This expected trend is clear in Fig. 3.2, even though the lengths sampled are modest.

3.3.2 Level statistics

Level statistics are frequently used to distinguish localized and thermal phases. For a Floquet system the eigenvalues of U are unimodular, so can be written in terms of phases θ_n as $e^{i\theta_n}$. We label the 2^L eigenvalues with integers n consecutively around the unit circle. A convenient measure of the level repulsion is [13, 26, 48] $r = \langle \overline{\min(\Delta\theta_n, \Delta\theta_{n+1})/\max(\Delta\theta_n, \Delta\theta_{n+1})} \rangle$, where $\Delta\theta_n = \theta_n - \theta_{n-1}$. In the localized phase, we expect $r \cong 0.39$ at large L following Poisson level statistics, while in the thermal phase we expect $r \cong 0.53$ at large L following circular orthogonal ensemble

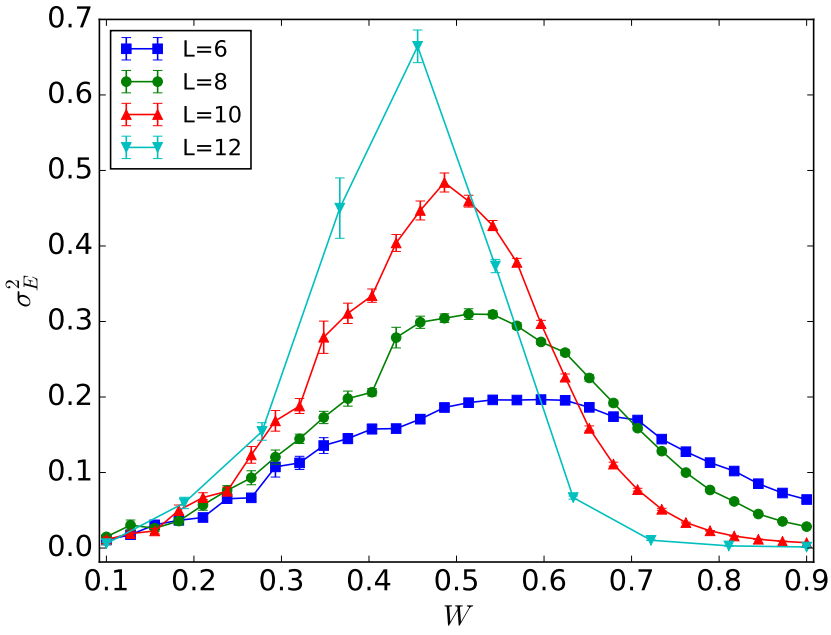

Figure 3.2: The variance σ_E^2 of the eigenstate entanglement entropy.

level statistics [1]. Results for this level statistics parameter r are shown in Fig. 3.3. It can be clearly seen that as the chain length L gets larger, r becomes a steeper function of W, and the system is well thermalized/localized at two ends of the range of W even for a size as small as $L = 10$. One may note that our model has an inversion symmetry about the center of the spin chain if we go to exactly $W = 1$ (no disorder), which would lead to accidental near-degeneracies between sectors of even and odd parities, disguising the level repulsion of thermal states. However, this is not a problem here, as Fig. 3.3 shows that the system is well thermalized by $W \simeq 0.9$ and still has enough disorder to guard against this inversion symmetry effect.

3.3.3 Correlation functions

Now we turn to the behavior of two long-distance correlation functions. The farthest distance in these spin chains with open boundary conditions is from the spin at one end of the chain to that at the other end. The end-to-end σ^z correlation averaged

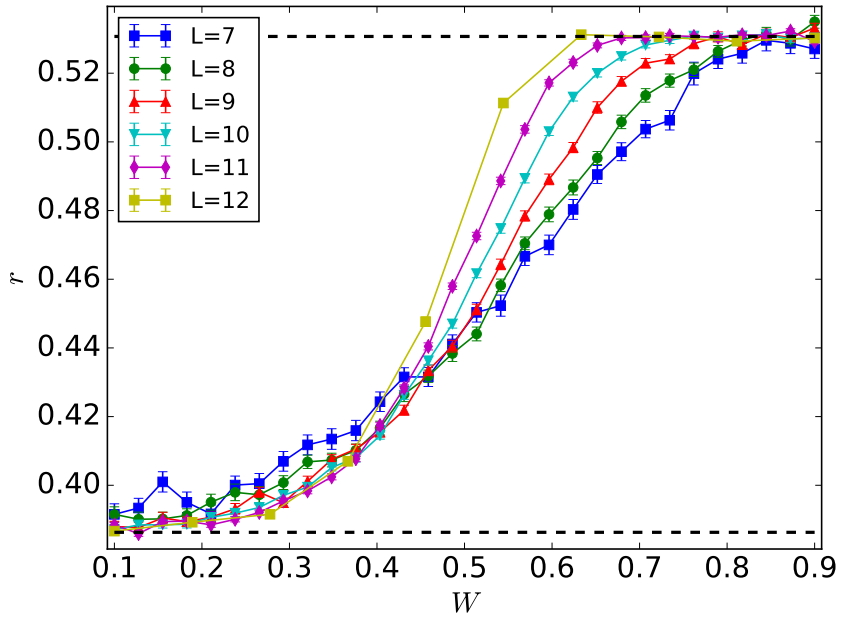

Figure 3.3: The level statistics parameter r of the eigenstates, as defined in the text. In the localized phase, r approaches $\cong 0.39$ at large L due to Poisson level statistics. In the thermal phase, the value approaches $\cong 0.53$ due to circular orthogonal ensemble statistics [1]. These two limiting values are indicated by the dashed lines.

over all eigenstates of U is

$$C_{zz} = \frac{1}{2^L} \sum_n \left(\langle n|\sigma_1^z \sigma_L^z|n\rangle - \langle n|\sigma_1^z|n\rangle \langle n|\sigma_L^z|n\rangle \right)^2 . \tag{3.5}$$

We also look at a four point unequal-time end-to-end σ^z correlation which is averaged over infinite time, so measures the "frozen correlations":

$$\begin{aligned} C_{zzt} = &\lim_{T\to\infty}\frac{1}{T}\int_T^{2T}\Big(\langle\sigma_1^z(0)\sigma_L^z(0)\sigma_1^z(t)\sigma_L^z(t)\rangle - \langle\sigma_1^z(0)\sigma_L^z(0)\rangle\langle\sigma_1^z(t)\sigma_L^z(t)\rangle \\ &- \langle\sigma_1^z(0)\sigma_1^z(t)\rangle\langle\sigma_L^z(0)\sigma_L^z(t)\rangle - \langle\sigma_1^z(0)\sigma_L^z(t)\rangle\langle\sigma_L^z(0)\sigma_1^z(t)\rangle\Big)dt \\ =&\frac{1}{2^L}\sum_n|\langle n|\sigma_1^z\sigma_L^z|n\rangle|^2 - \left(\frac{1}{2^L}\sum_n|\langle n|\sigma_1^z|n\rangle|^2\right)\left(\frac{1}{2^L}\sum_n|\langle n|\sigma_L^z|n\rangle|^2\right) \\ &- \left(\frac{1}{2^L}\sum_n\langle n|\sigma_1^z|n\rangle\langle n|\sigma_L^z|n\rangle\right)^2 - \frac{1}{2^{2L}}\sum_{n\neq m}\big(|\langle n|\sigma_1^z|m\rangle|^2|\langle n|\sigma_L^z|m\rangle|^2 \\ &+\langle n|\sigma_1^z|m\rangle^2\langle m|\sigma_L^z|n\rangle^2\big)\ , \end{aligned} \tag{3.6}$$

where L is the length of the system and $\{|n\rangle\}_n$ is the set of all eigenstates of U. Here $\langle\cdots\rangle$ means the average over an infinite temperature ensemble with density matrix $I/2^L$. σ_1^z and σ_L^z are the Pauli matrices at two ends of the spin chain and $\sigma_1^z(t)$ as well as $\sigma_L^z(t)$ are these two operators under the Heisenberg picture at time t. The two point correlation function measures the square of the fluctuation from the two end spins averaged over all eigenstates. For fully localized or thermal eigenstates, the fluctuation should be exponentially suppressed by the length of the chain, so C_{zz} should be negligible in these two regimes when the system is large enough. As we approach the transition point from both sides, since correlation length increases, C_{zz} should also increase and in the infinitely large system, there would be a peak at the transition point. Similarly, C_{zzt} measures the correlation of fluctuation over time. It is small in both thermal phase, because of the short correlation length in time for thermal states, and localized phase, because of the small magnitude of the fluctuation itself. As we approach the transition point, a peak is expected due to the increase in fluctuation and correlation length in time.

The peaks of these two correlation functions are difficult to observe in Hamiltonian systems because of the presence of conservation laws which hinders the thermalization

of the system [43]. This creates a noisy background in thermal regimes, and since at finite size the transition point is in the thermal phase, this makes localizing the peak more difficult. Fig. 3.4 shows the two correlations for a "standard" Hamiltonian model [13] frequently used in MBL phase transition studies:

$$H = \sum_{i=1}^{L} \left(h_i S_i^z + \vec{S}_i \cdot \vec{S}_{i+1} \right) \tag{3.7}$$

with h_i being uniformly random on $[-W, W]$. In Fig. 3.4(a) the peak of C_{zz} is just barely visible at $L = 14$; the failure to thermalize the system at small W creates large residual correlations which hides the peak. The situation of C_{zzt} is better: the peak becomes visible around $L = 10$ but may only be good enough for analysis around $L = 12$. On the other hand, in the Floquet system, as it is better thermalized at finite size, we would obtain a better signal-to-noise ratio at smaller sizes. The numerical results are shown in Fig. 3.5, where each point is an average over independent realizations and error bars represent statistical errors. Up to $L = 11$ there are 100 realizations and at $L = 12$ there are 50 realizations. Large values can still be observed in the thermal phase due to finite size effect at small L, but these values decrease exponentially as L increases. For C_{zz} peaks become quite obvious for $L \gtrsim 9$ and for C_{zzt} even $L = 7$ gives a reasonable peak to analyze: the situations at finite size are thus much better than those under the Hamiltonian dynamics. As system size increases, these peaks gradually move to the localized side as expected, and it is interesting to note that starting around $L = 9$ the peak height no longer decreases. As these peaks are much narrower than those from variance of entanglement entropy, further investigations of them with finite size scaling can certainly aid in finding the transition point more accurately.

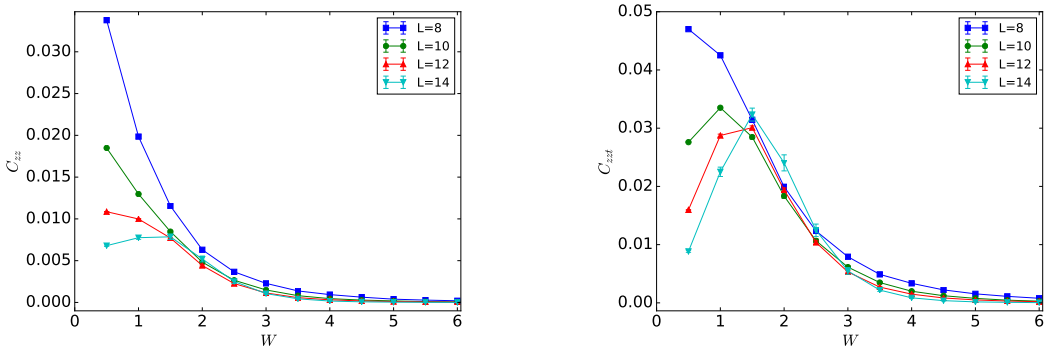

(a) (b)

Figure 3.4: Numeric results of the two correlation functions defined in the text for Hamiltonian (3.7). The peak indicates the transition between localized phase and thermal phase. (a) shows the equal time two point correlation C_{zz} and (b) shows the four point time correlation C_{zzt}.

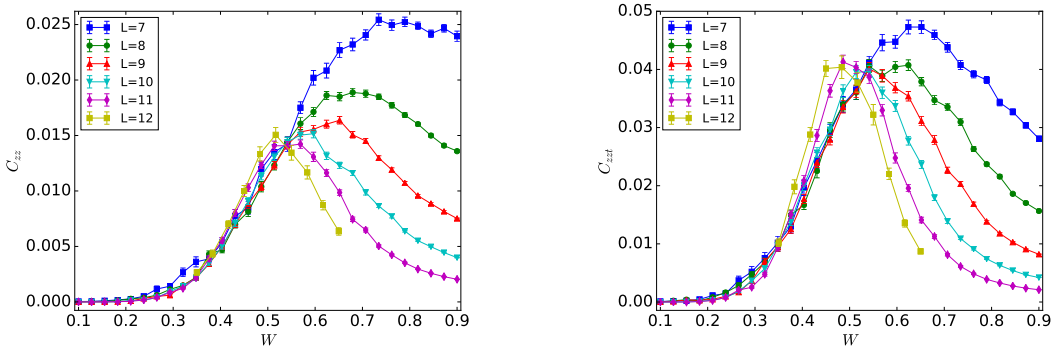

(a) (b)

Figure 3.5: Numeric results of the two correlation functions defined in the text for our Floquet model. (a) shows the equal time two point correlation C_{zz} and (b) shows the four point time correlation C_{zzt}.

3.3.4 Linked cluster expansion

Recently Ref. [60] proposed a numerical linked cluster expansion study of entanglement entropy to obtain an estimation of the upper bound of the transition point. Here we apply the same calculation to our Floquet model at infinite temperature. Following Ref. [60], we define

$$a_n = \sum_{c,|c|=n} \tilde{S}(c), \qquad \tilde{S}(c) = S(c) - \sum_{c' \subset c} \tilde{S}(c') \tag{3.8}$$

at an order n, where $S(c)$ is the bipartite von Neumann entropy across a pre-defined cut for a set of connected sites c across the cut, averaged over all eigenstates. Following Ref. [60], the disorder averaging over 5000 realizations is performed before the subgraph subtraction. For thermal states following volume law entanglement, a_n is expected to saturate to $1/2$ for high enough n [60]. In the localized phase, a_n is expected to decay exponentially to 0 when n is larger than some correlation length, so an extrapolation of $a_\infty \geq 0$ corresponds to a breakdown of area law of entanglement entropy [60]. The results for our model are shown in Fig. 3.6. As $W \to 1$, a_n gradually settles down to about $1/2$, demonstrating that our system is well thermalized in this region. On the other end, as $W \to 0$, a_n steadily decreases, consistent with a transition from volume law entanglement to area law entanglement. For small enough W, we can see a_n suggests an extrapolation with $a_\infty = 0$, indicating the entry into localized regimes. The upper bound for our transition thus can be crudely estimated as $W \lesssim 0.36$.

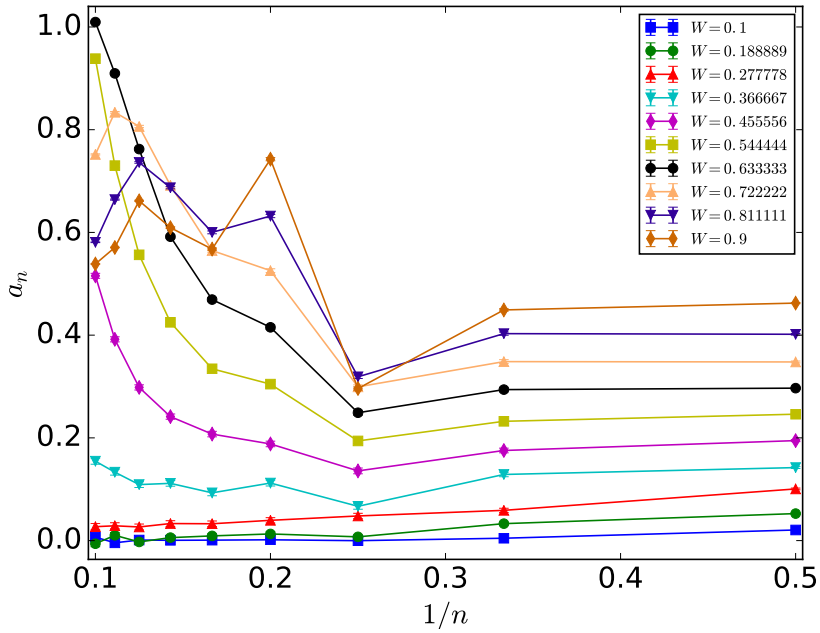

Figure 3.6: Numeric linked cluster expansion for the entanglement entropy. In the thermal phase, a_n would approach $1/2$ as $n \to \infty$, and in the localized phase a_n would decrease exponentially to 0 for large enough n.

3.4 Preliminary Finite Size Analysis

3.4.1 Different System Sizes

To get a further understanding of the two correlations, we can study the end-to-end correlations versus different systems sizes. In the following, each point shown is an average over 100 realizations of random disorders for $L \leq 11$ and 50 realizations for $L = 12$. Fig. 3.7 demonstrates the results in the thermal region ($W = 0.9$) and Fig. 3.8 plots the MBL region ($W = 0.2$). One may notice the rather nosisy results for C_{zz} and C_{zzt} in localized regions. This may come from the broad distributions of correlations among different eigenstates, which make the sample mean taken here converges slowly to the true mean value. To get a better statistics, we can define the

log zz correlation square:

$$L_{zz} = \sum_n \ln\left(\langle n|\sigma_1^z\sigma_L^z|n\rangle - \langle n|\sigma_1^z|n\rangle\langle n|\sigma_L^z|n\rangle\right)^2/2^L. \tag{3.9}$$

which will have a narrower distribution. According to Jensen's inequality, this would be smaller than taking the logarithm of C_{zz} directly. We do not define similar quantity for C_{zzt} as the mix of eigenstates in Eq. (3.6) makes the definition more difficult. In the thermal region, an exponential relation is present for both zz correlation square C_{zz} and log zz correlation square L_{zz} with similar exponents (-0.58 ± 0.01 for C_{zz}, and -0.56 ± 0.02 for the slope of L_{zz}), consistent with our expectation that small variance of correlations among eigenstates leads to similar results in these two methods. On the other hand, in the MBL region, the raw C_{zz} gives a relatively poor exponential relation while L_{zz} still gives a quite straight line with a slope -1.78 ± 0.05. Therefore we see that the decay in the MBL region for the end-to-end correlation is much shaper, suggesting a much smaller finite size noise in the localized region, consistent with our observation. In the thermal region, the time correlation C_{zzt} also behaves nicely, exhibiting an exponential relation with system sizes, and the exponent -0.61 ± 0.01 from a simple linear fitting is also similar to what is seen for C_{zz}. However, in the MBL region, C_{zzt} behaves rather irregularly under different system sizes.

Fig. 3.9 shows C_{zz} and L_{zz} in the transition region around $W = 0.3$ and $W = 0.4$. Fig. 3.9(a) shows C_{zz} from the thermal region to where the transition roughly happens, while Fig. 3.9(b) gives the correlation from the thermal to the localized region. Fig. 3.9(c) shows L_{zz} from the transition to MBL region, while Fig. 3.9(d) plots L_{zz} in the whole region. As we gradually move out of the thermal region, at large L, correlation decays slower as system sizes increases, and then starts to increase when we approach the critical point, which generates the peaks we observe. When we gradually move into the localized region, an exponential decay emerges again. At

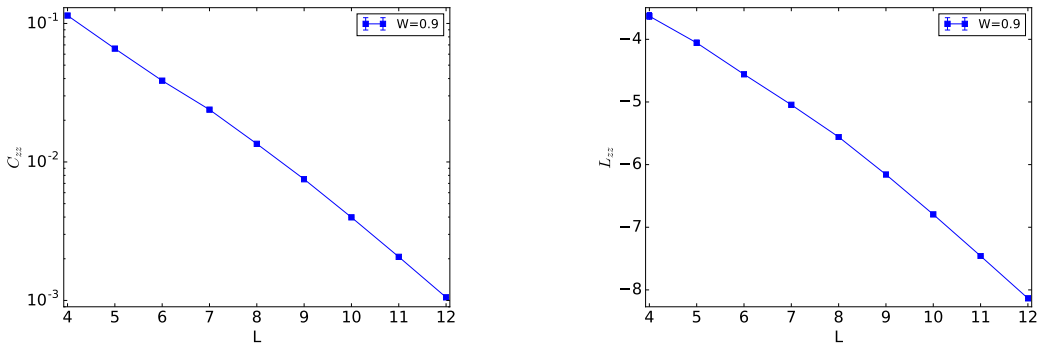

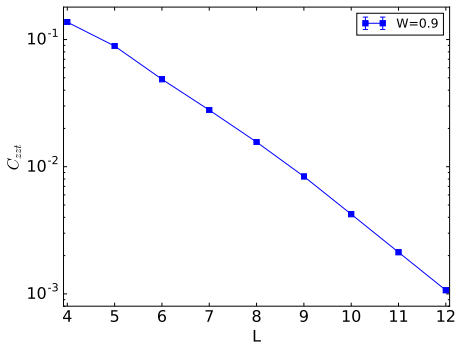

Figure 3.7: End-to-end correlations versus system size L at $W = 0.9$ in the thermal region.

small L, the correlation always decreases as we increase W, thus giving no peaks. This difference between different system sizes may result from the finite correlation length probed at these points.

3.4.2 Different Separation Between Spins

To further study the properties of the correlations, we can investigate C_{zz} with different spin separations: for a given distance r, we can change σ_1^z and σ_L^z in Eq. 3.5 to two spins which have r extra bonds between them, and for simplicity we only study patterns that are symmetric about the spin chain center. Under this notation, $r = 1$ represent two adjacent center spins and with $r = L - 1$ we go back to our original

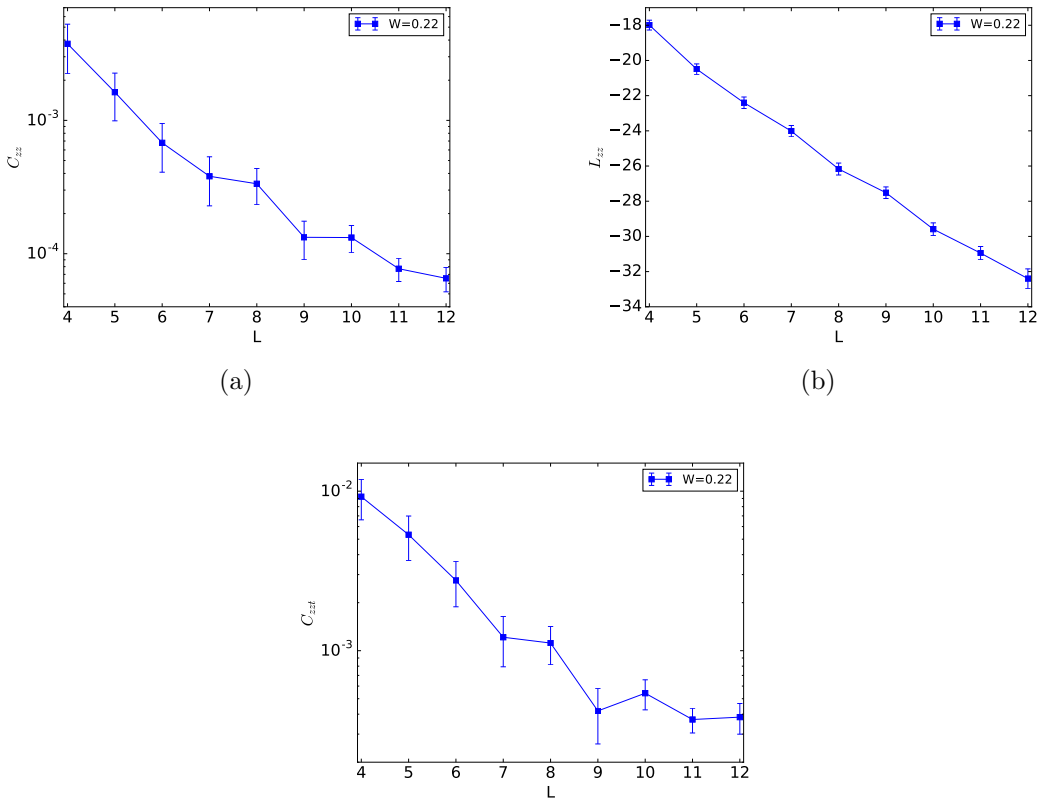

Figure 3.8: End-to-end correlations versus system size L at $W = 0.22$ in the localized region.

C_{zz}. In the following, every point in the plots is averaged over 500 realizations for $L \leq 8$, 100 realizations for $L = 9\,, 10\,, 11$ and 50 realizations for $L = 12$. Fig. 3.10 and Fig. 3.11 demonstrate the relation between correlation and the separation r with various system sizes in the thermal region ($W = 0.9$) and MBL region ($W = 0.2$). In the thermal region, the correlation is roughly independent of r except when r is small, and the flatness at moderately large r increases as system sizes L increases. This is consistent with our expectation that eigenstates are extended in the thermal region so the correlation should not decay. In the MBL region on the other hand, all correlations show an exponential decay with r, consistent with the picture of localized eigenstates. It is interesting to note that as L increases, the decreasing rate slows down. Presumably, the diminishing decrease rate should converge to some finite value

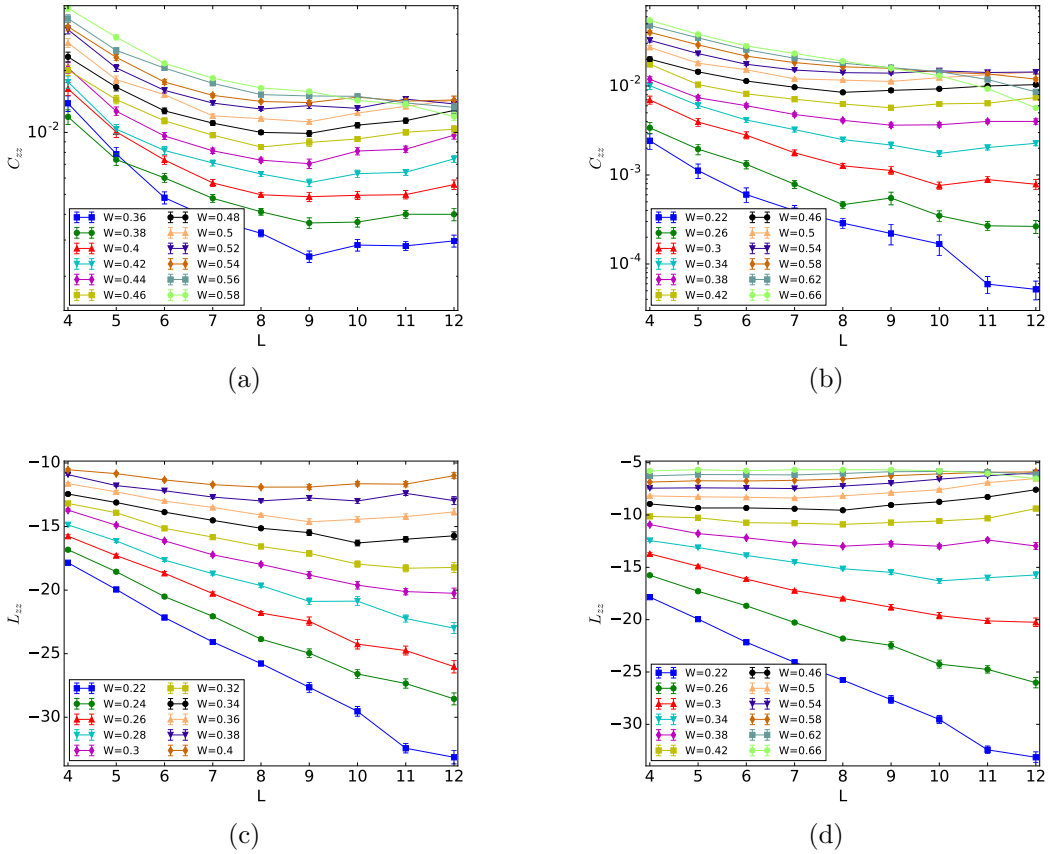

Figure 3.9: End-to-end C_{zz} versus system sizes L inside the transition region.

as $L \to \infty$ so that in the thermal dynamic limit C_{zz} still decreases exponentially with r. In either case, we can see that the end-to-end correlation decreases as L increases, consistent with what we observed above. For L_{zz}, analog behaviors are observed.

Fig. 3.12 shows the relation between L_{zz} and r in the transition region of different W. As we go into transition region from the localized side, systems at large length start to flatten the exponential decay of correlations, and in the mean time the correlation curve as a whole starts to drift down. It seems that the combination of flattening and decrease in value results in similar peak heights of end-to-end correlations during the transition at different lengths, as the decay of correlations tends to drag the peak down, while the flattening tends to push it up. Meanwhile, we can also see that at large L, for some W on the thermal side, the correlation may even increase

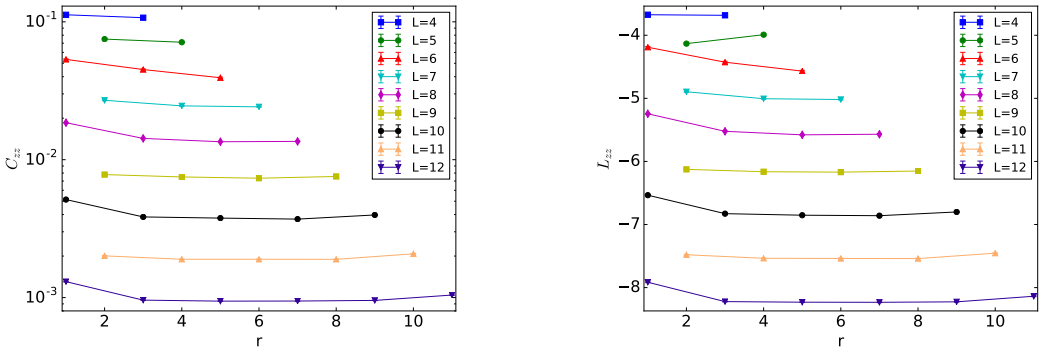

(a) (b)

Figure 3.10: Relation between correlations and the separation r (number of bonds) between two spins symmetric about the spin chain center at $W = 0.9$ in the thermal region for different L.

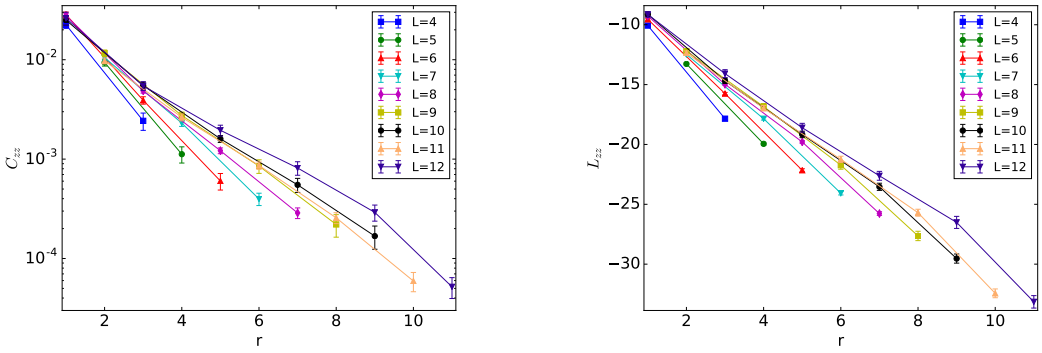

(a) (b)

Figure 3.11: Relation between correlations and the separation r (number of bonds) between two spins at $W = 0.22$ in the MBL region for different L.

at large r, similar to what we observed in Fig. 3.9. This may come from our use of open boundary condition, which makes spins closer to two ends different compared to spins near the center. Thus when eigenstates are still not fully extended, the spins at two ends are more localized than those in the middle. As we move further into the thermal phase, this particular behavior at large r diminishes. Fig. 3.13 shows the change of correlation in the transition zone at $L = 12$, which gives a more clear picture of change of correlations from MBL phase to thermal phase, particularly, the flattening of correlations, and the non-monotonic behavior in r when W increases.

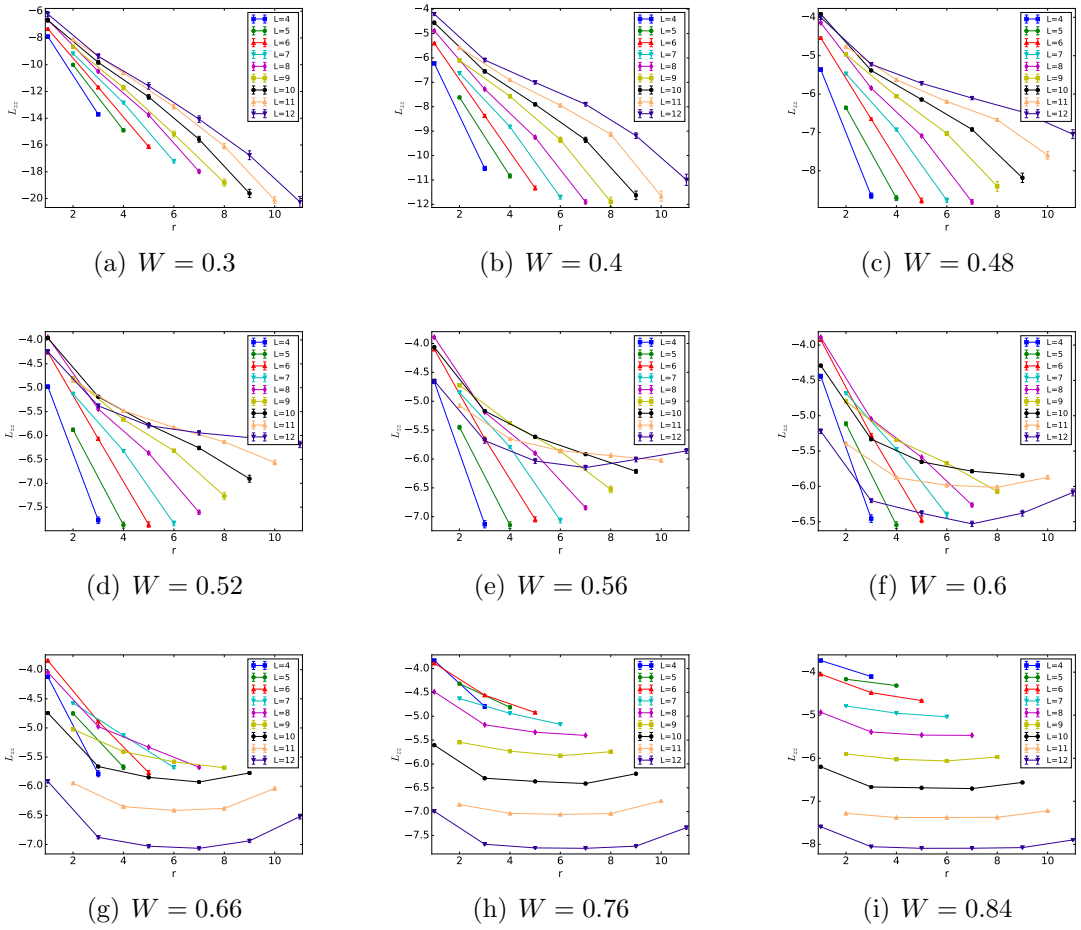

(a) $W = 0.3$ (b) $W = 0.4$ (c) $W = 0.48$

(d) $W = 0.52$ (e) $W = 0.56$ (f) $W = 0.6$

(g) $W = 0.66$ (h) $W = 0.76$ (i) $W = 0.84$

Figure 3.12: Relation between correlations and separation r of spins in the transition region for different system sizes.

Now we show our attempt to obtain exponent components based on the scaling we have observed. At the true critical point W_c of the infinite system, we expect the

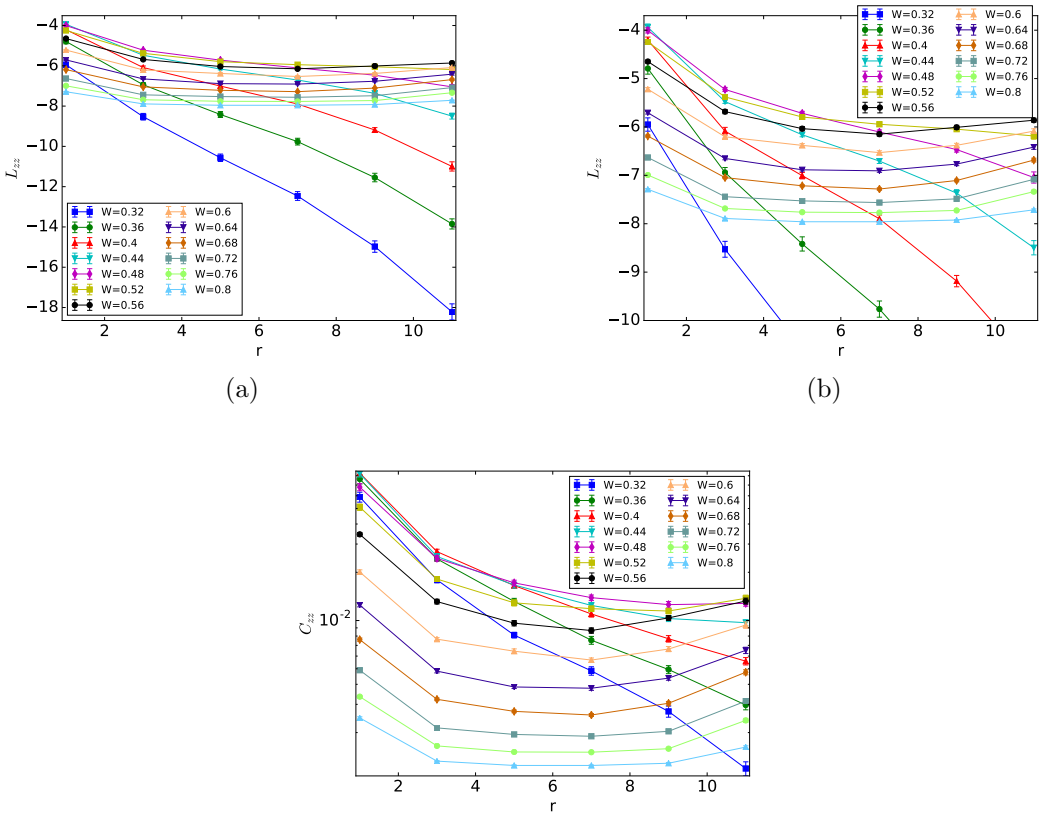

Figure 3.13: Relation between correlations and separation r in the transition region for $L = 12$.

correlation function to follow

$$C_L(r) \simeq r^{\eta} f(r/L) = L^{\eta} g(r/L) \cong L^{\eta} g\left(\frac{r}{L-1}\right) \tag{3.10}$$

for relatively large L, so we should see a power law in L by plotting end-to-end correlation $C_L(r = L - 1)$. Because we expect the critical point to be within the MBL phase, to have better statistics, we will focus on the log zz correlation square L_{zz}, so in the following $C_L(r) \equiv L_{zz}(r, L)$. To reduce the pollution from finite size effect, we only consider system sizes $L \geq 8$ and apart from $L = 12$, all points are averaged over 100 runs, and for $L = 12$, points are averaged over 50 runs. The log-log plot (or more precisely semi-log plot for the log zz correlation square) is shown in

Fig. 3.14(a). It can be seen that from $W = 0.2$ to $W = 0.3$ they all demonstrate somewhat straight lines, possibly due to the small number of points we have. If we expect the critical point to be not that far into the MBL phase, given that at $L = 12$ the peak is at about $W = 0.5$, we may say $W_c \simeq 0.3$ as it is the largest W in the plot which shows a reasonable linear behavior. Linear regression at $W = 0.3$ gives $\eta \simeq -6.29 \pm 0.16$. Fig. 3.14(b) gives $C_L(r) \times L^{-\eta}$ in the log-log plot, which, if plotted against $r/(L-1)$, should collapse to a single line with different L if our scaling assumption is correct. It can be seen that curves are still far apart from each other with $\eta = -6.295$. In fact, if we use a different power $\eta \simeq -2$ in Fig. 3.14(c), the curves collapse much better. This suggests our data may still be heavily influenced by finite size effect, possibly because the use of only end-to-end spins, which feel the boundaries of the system strongly.

If we use more spins on the spin chain, we can also directly search different W and η to find the best "collapse" of $C_L(r)$ in terms of $r/(L-1)$ as in Fig. 3.14(c), though the difficulty lies in how to define a reasonable measure of the goodness G of the "collapse". One straightforward way is to construct a "base curve" in the plot and compute the "distance" from all curves to this base curve. Note each curve represents $C_L(r)$ at some integer $r \leq L$ for a fixed L. Here at a given η and W, we construct the base curve using points from $L = 12$ as base points since this case has the most points. The base curve is defined as $\tilde{h}_{12}(x) = \tilde{h}_{12}(\frac{r}{11}) = C_{12}(r) \times 12^{-\eta}$ with linear interpolation between all the base points. For another L and r', we then have a point $h_L(x') = h_L(\frac{r'}{L-1}) = C_L(r') \times L^{-\eta}$ at $x' = r'/(L-1)$ and can compute its distance to the base curve by $d_L(r') = \left| h_L(x') - \tilde{h}_{12}(x') \right|$. The distance from a given curve with a fixed L to the base curve is thus characterized by distances of all the sampled points from this curve to the base curve. We then define the goodness of collapse at a given η and W to be $G(\eta, W) = \frac{1}{m} \sum_L \sum_r d_L(r)^2$, where m is the total number of different curves. As above only systems with sizes between 8 and 12 are considered

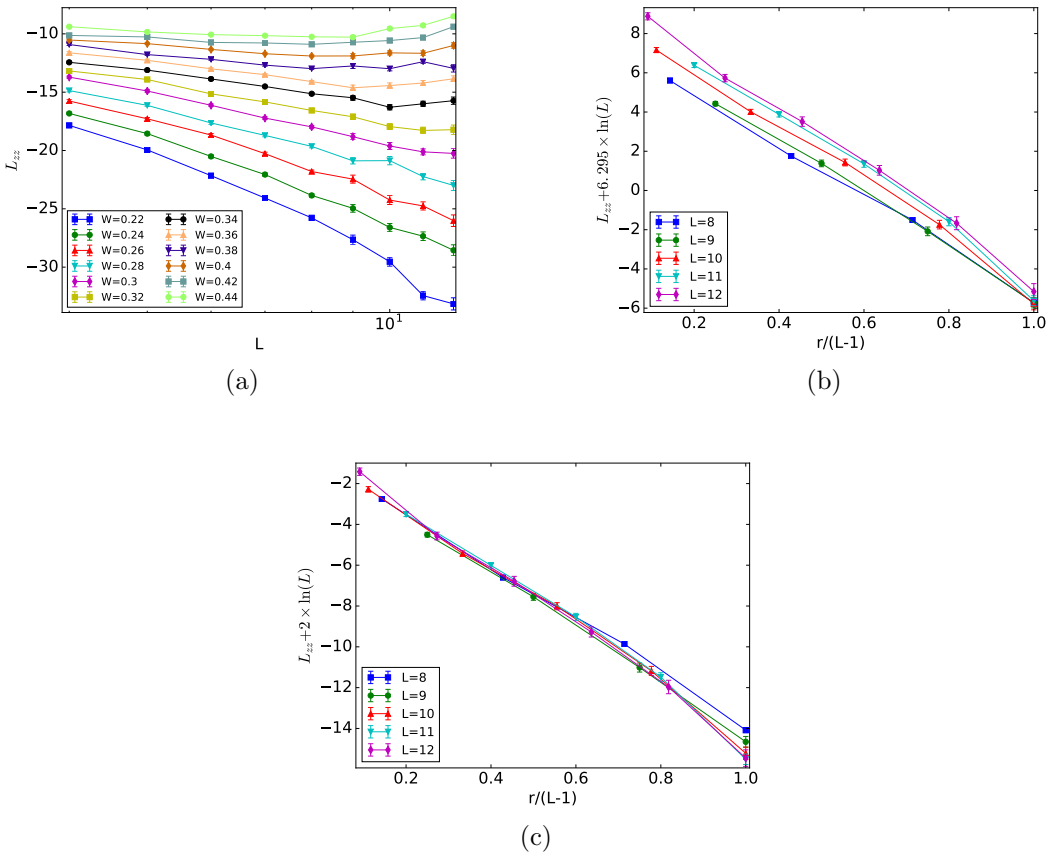

Figure 3.14: (a) shows the end-to-end L_{zz} against the logarithm of system size L. (b) shows the collapse of data at $W = 0.3$ with a fitted power $\eta = -6.295$, and (c) shows the collapse with another power $\eta = -2$.

in this calculation. The 3D plot of G is shown in Fig. 3.15(a). Fig. 3.15(b) shows the lowest G^* at a given W and Fig. 3.15(c) illustrates the "best" η^* that gives rise to G^* at a given W. It can be seen that between $W = 0.36$ and $W = 0.5$, the best collapse is achieved by having a positive η, which seems physically unreasonable. The global minimum is found at $W = 0.36$ and $\eta = 1.0$, which is barely within the bound set in Section 3.3.4 but with an unphysical exponent, suggesting we possibly should not take these numbers too seriously. Fig. 3.15(d) gives the collapse with $\eta = 1.0$ at $W = 0.36$, which is actually not bad. To avoid the seemingly unphysical positive η, we may assume that in this case we actually have $\eta \simeq 0$ and the not large positive number is caused by statistical errors. Fig. 3.15(e) then gives the collapse with $\eta = 0$

at $W = 0.36$, which is still reasonable. This seems to suggest that the actual η may be quite close to 0, and we may just directly search the "best" collapse by using $\eta = 0$ in the above. The results are shown in Fig. 3.16. A local minimum is still formed around $W \simeq 0.36$, though in this case $W = 0.38$ has the lowest value, and violates the bound seen in Section 3.3.4, thus possibly not accurate. Nevertheless, we still plot the collapse in Fig. 3.16(b) with $W = 0.38$ which is also pretty good. On the other hand, we may also do the same search for the best power η^* and critical point W_c but restricting $\eta \leq 0$. The results are shown in Fig. 3.17. The best collapse is found at $\eta = 0$ and $W_c = 0.38$, but in general it seems any W between 032 and 0.38 can be candidates for W_c.

The above analysis suggests the difficulty in locating η, so if we just want to estimate W_c, instead of imposing $\eta = 0$ or $\eta \leq 0$ by hand, we may abandon finding it at all and assume a more general scaling form

$$C_L(r) \simeq A_L g(\frac{r}{L-1}) \tag{3.11}$$

at the critical point for the correlation, and we can directly search for a W where curves are "best parallel" to each other. Without using any further knowledge about the shapes of curves, we can again use $L = 12$ to construct a base curve $\tilde{h}_{12}(x) = \tilde{h}(\frac{r}{11}) = C_{12}(r)$ with linear interpolation, and similarly define (signed) distance to this base curve from a point with given L and r' as $d_L(r') = h_L(x') - \tilde{h}_{12}(x')$ with $h_L(x') = C_L(r')$ and $x' = r'/(L-1)$. The goodness of being parallel is then $G_P(W) = \sum_L \sigma^2(d_L) \times N_L$, where $\sigma^2(d_L)$ is the variance of all the distances at a fixed L to the base curve, and N_L is the number of points at that L. Here for simplicity, we ignore any normalization constant. This gives us a rather general measure of "paralleness" of curves applicable to any set of curves. On the other hand, if we are within MBL phase, as we suspect of the W_c, the curves are almost simple exponential in r at a fixed

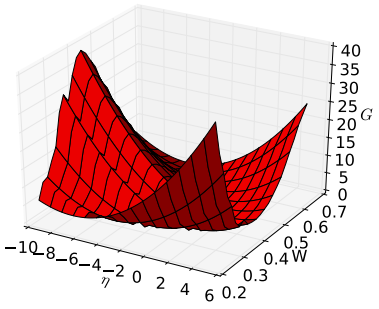

(a)

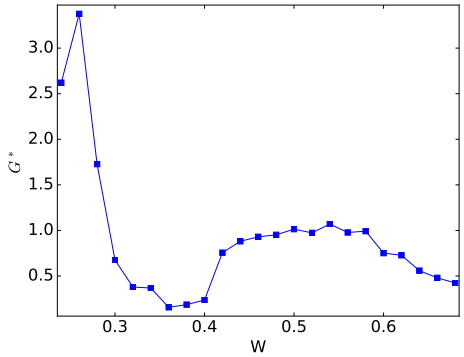

(b)

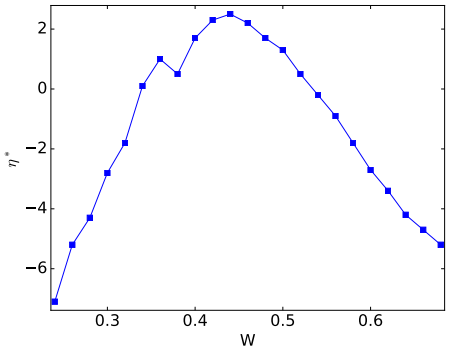

(c)

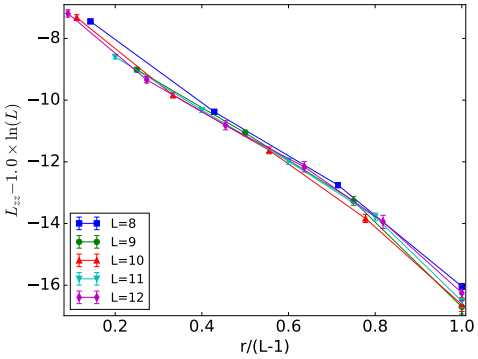

(d)

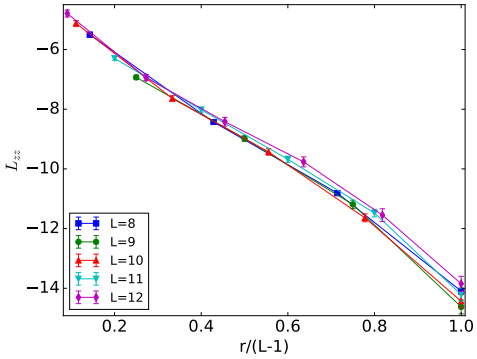

(e)

Figure 3.15: The search for the best η and W given a measure of goodness G for data collapse defined in the text. (a) shows the 3D plot of the goodness and (b) gives the smallest G at each W. (c) maps out the best η corresponding to each G^* and (d) shows the collapse of the data at the best combination found: $W = 0.36$, $\eta = 1.0$. (e) shows the collapse at $W = 0.36$ and $\eta = 0$.

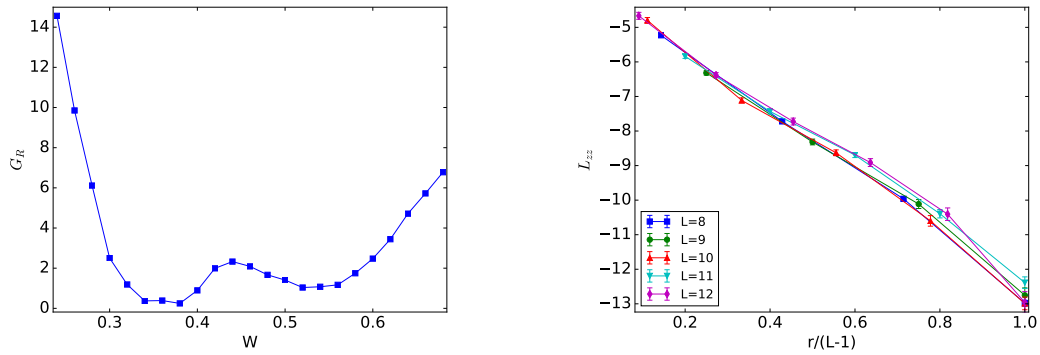

(a) (b)

Figure 3.16: The search for the best W of data collapse at $\eta = 0$. (a) shows the goodness of collapse which has a minimum at $W = 0.38$, and (b) plots the collapse at $W = 0.38$.

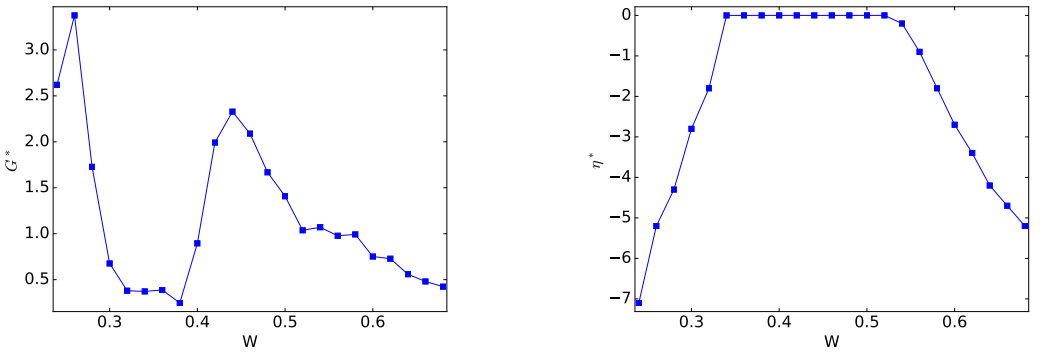

(a) (b)

Figure 3.17: (a) shows the goodness of collapse for different choices of η and W_c with the requirement that $\eta \leq 0$. (b) gives the best η for each W_c.

L, so we can also judge the quality of being parallel by investigating the variances of slopes in the log-log plot, which is much easier and possibly more accurate than the generic way mentioned above. Particularly, we can define the goodness of being parallel at a given W as $G_L(W) = \sigma^2(\tilde{s}_L)$, i.e., variance of scaled slopes at different L, where the scaled slope at a given L is defined as $\tilde{s}_L = \hat{b}_1/R^2$, with $\hat{b}_1$ being the fitted slope in the log-log plot and R^2 indicating the goodness of fit. Presumably, these scaled slopes can be used to punish the curves which are not very linear. The goodness from these two methods are shown in Fig. 3.18(a) and Fig. 3.18(b), and both give a global minimum at $W = 0.36$. As expected, the two measures resemble each other for small W where the system is in localized phase, but surprisingly also similar for relatively large W where correlations $C_L(r)$ may not be simple exponential in r. Besides, they look similar to Fig. 3.15(b), which suggests that when curves do not collapse, they also tend to not be parallel to each other. Combining the results above, it seems the critical point may be around $W = 0.36$. If we still believe in the scaling form $C_L(r) \simeq L^{\eta} g(\frac{r}{L-1})$ and η cannot be positive, then $\eta \simeq 0$ or may be just a small negative number at the critical point. The small magnitude of η is also consistent with our difficulty in seeing the decrease of peak heights for large L when they are reasonably close to the true critical point.

3.4.3 Distance to Correlation Peaks

Another scaling law that may be of interest in the MBL phase transition involves positions of peaks of correlations: $|W_{peak}(L) - W_c| \sim L^{-1/\nu}$, and we may estimate ν by investigating $|W_{peak}(L) - W_c|$ in a log-log plot versus L. One estimation of errors for locating correlation peaks can be written as $\max\{d_p, d_{nn}\}$. Here d_{nn} is the distance from the peak point to its nearest neighboring W used and thus comes from our discrete sampling of disorder strength W. d_p, on the other hand, represents the error associated with statistical uncertainties of correlation values, which come from

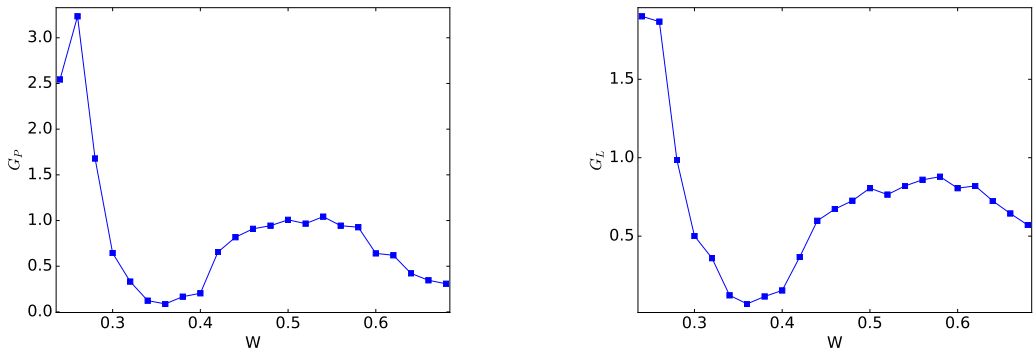

(a) (b)

Figure 3.18: The search for the best W where data curves are most parallel to each other. In (a) a general goodness is demonstrated and in (b) the goodness is based on the assumption that data curves for a given L are roughly exponential in r.

finite number of realizations of disorders. Particularly, if we denote the uncertainty for a correlation value $C_L(W)$ as $\delta C_L(W)$ and an estimated peak position as W_{peak}, then we can define a set of W as $\mathcal{C} = \{\text{sampled } W | C_L(W) + \delta C_L(W) \geq C_L(W_{peak}) - \delta C_L(W_{peak})\}$, so that

$$d_p = \max_{W \in \mathcal{C}} |W - W_{peak}| \tag{3.12}$$

From Fig. 3.5(a) and Fig. 3.5(b) it can be observed that $\delta C_L(W)$ is usually larger around W_{peak} than deep in the phase, so d_p may become a more serious problem than d_{nn} if we do not have large enough realizations. Another error in estimating ν comes from the small sample size of W_{peak}, and it can only be reduced by having more system sizes. This illustrates the small advantage brought by our model: since given current computational power we can only perform exact diagonalization at $L \simeq 18$, being able to identify peaks at smaller L would slightly improve our accuracy. In the following, we would only reduce d_{nn} by performing a finner sampling of W in regions around peaks suggested by Fig. 3.5(a) and Fig. 3.5(b), and keep the same number of runs up to $L = 12$, so our results can only serve as a demonstration rather than providing an accurate numeric estimation of ν.

Fig. 3.19(a) and Fig. 3.20(a) illustrate C_{zz} and C_{zzt} with statistical errors for $L \geq 7$. W_{peak} are found as the W which gives the largest correlation values, and also reported in the plots. It can be seen that in our case d_p is much larger than d_{nn} and thus severely constrains the accuracy of our results. Since peaks are still in the thermal region, there would be not much difference between C_{zz} and L_{zz}, so only the former is considered. $|W_c - W_{peak}|$ against system size L at different W_c are shown in a log-log plot at Fig. 3.19(b) for C_{zz} and Fig. 3.20(b) for C_{zzt}. The roughly straight lines suggest our estimation of W_{peak} are not too bad for C_{zz} but interestingly not for C_{zzt}, so in the following we will only focus on C_{zz}. The two points $L = 7$ and $L = 12$ are particularly off the trend from Fig. 3.19(b). This is understandable as at $L = 7$ the peak in C_{zz} is only barely identifiable and we only have 50 realizations at $L = 12$. However, the major difficulty in estimating W_c is that all lines are look straight. We know that when $W_c \to \infty$, all points would lie on a flat line, but it also seems as W_c decreases, we are still left with straight lines, just with steeper slopes. Why the "near" power-law relations would prevail in a range of W_c, if it is not an artifact of our numerical computation, still eludes us. The linear regression results are shown in Table. 3.1 for C_{zz}, where $L = 7$ points are excluded in the hope to slightly increase the accuracy. If we can still interpret R^2 as a representation of linearity in our small sample analysis, then we see as W_c increases, the linearity worsens, though seems at a slower rate at $W_c \simeq 0.37$. If this boundary is real, then it possibly can be used to pick $W_c \simeq 0.37$ as our critical point, and in this case it is just barely consistent with our estimation in Section 3.4.2. The power around this W_c is $\nu \simeq 0.6$ for C_{zz}, which strongly violates the Chayes inequality [64, 69] in one dimension with $\nu \geq 2$, and this is also observed in some other numerical studies [51, 57]. As we mentioned earlier, we should not read too much into this preliminary analysis.

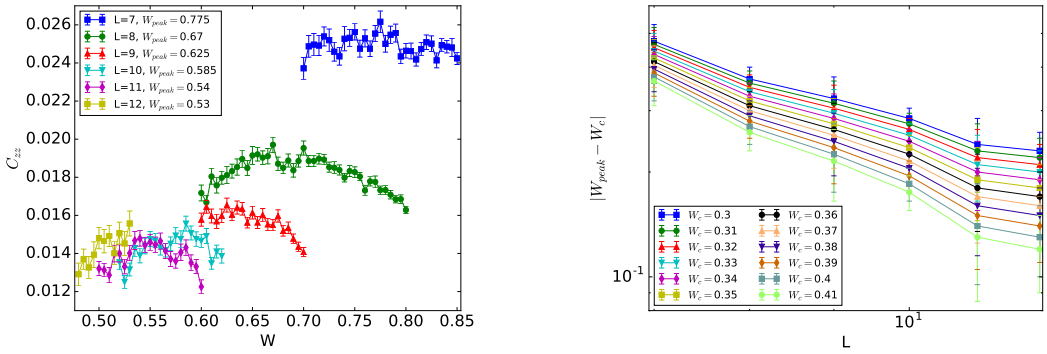

(a) (b)

Figure 3.19: The peak positions from C_{zz} with a finer sampling and the scaling with different choices of W_c.

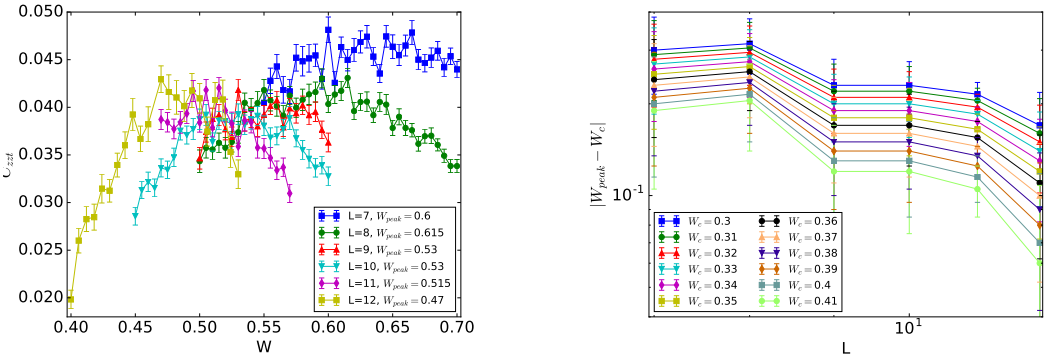

(a) (b)

Figure 3.20: The peak positions from C_{zzt} with a finer sampling and the scaling with different choices of W_c.

W_c	ν	R^2	W_c	ν	R^2
0.3	0.81 ± 0.06	0.9838	0.31	0.78 ± 0.06	0.9837
0.32	0.75 ± 0.06	0.9836	0.33	0.72 ± 0.05	0.9835
0.34	0.69 ± 0.05	0.9834	0.35	0.66 ± 0.05	0.9832
0.36	0.64 ± 0.05	0.9831	0.37	0.61 ± 0.05	0.9829
0.38	0.58 ± 0.04	0.9826	0.39	0.55 ± 0.04	0.9823
0.4	0.52 ± 0.04	0.9819	0.41	0.49 ± 0.04	0.9815

Table 3.1: Fitted slopes from C_{zz} scaling points in Fig. 3.19(b) excluding $L = 7$.

3.5 Conclusion

In this chapter, we propose a one-dimensional disordered Floquet model which can be used for numerical studies of the phase transition between the thermal phase and the MBL phase. Because of the lack of conservation laws, the Floquet model is better thermalized compared to Hamiltonian models at finite size, providing a better signal-to-noise ratio in the thermal phase, thus more suitable for finite size investigation as usually at finite size the transition occurs in thermal regimes. Here we calculated various popular quantities that are used for the characterization of the transition for our model, and they all confirm that our model can have both a well localized phase and a well thermalized phase even at a relative small size. Thus our model can be a good candidate used for more accurate numerical investigation of the MBL phase transition. We further show some preliminary results on finite size scaling using correlation functions. Assuming a scaling form Eq. (3.5), the results suggest a transition point $W_C \simeq 0.36$ and a possible exponent component $\eta \simeq 0$, though our analysis is still affected by possible finite size effect and we only crudely sampled the interested region. We also investigate another scaling equation (3.12). It roughly gives the same W_c as above, but given our setup it is too inaccurate to draw any quantitative conclusion. A more thorough and careful numerical finite size studies using the model proposed in this chapter can be a future project which may quantitatively provides more insight into the MBL phase transition.

Chapter 4

Many-body localization phase transition: a new simplified approximate renormalization group

4.1 Introduction

In the previous chapter we showed some numerical investigation of the phase transition between many-body localization (MBL) and thermalization. In this chapter, we will take another look at it from a different approach. The MBL phase transition is a dynamical quantum phase transition which appears to be a completely new type of quantum phase transition [2, 13, 25, 26, 41, 50–65, 70]. It occurs in the thermodynamic limit of large systems for certain closed quantum many-body systems with quenched disorder. It separates the *thermal phase* where the closed system serves as a "bath" for itself and at long times approaches thermal equilibrium at a nonzero temperature and thus a state described by equilibrium quantum statistical mechanics, from the *MBL phase* where these statements are not true and instead the system remains localized near its initial state. Thus it is a phase transition where the long-time behavior

of the system stops being given by equilibrium quantum statistical mechanics. It is also an "eigenstate phase transition" [71], where the nature of the eigenstates of the system's dynamics changes from thermal and volume-law entangled, to localized and boundary-law entangled.

Many questions remain unanswered about this MBL phase transition. A theoretical tool that has been highly successful in understanding more "traditional" classical and quantum phase transitions and critical systems is the renormalization group (RG). Two recent papers have formulated and studied approximate RG treatments of the MBL phase transition in one-dimensional systems [41,54]. In the present chapter, we simplify these RG approaches even more, allowing a more exact study of the resulting fixed point and phase transition within our simplified RG [70]. These approximate RG's can serve at least two purposes: (i) as examples that suggest possible properties of these phases and this phase transition, and (ii) as first steps towards possibly developing a more systematic RG treatment of these systems.

One feature of our RG that we highlight, since it was not emphasized in the previous RG studies [41, 54] nor in the recent study of Griffiths effects in the MBL phase [59], is the possibility that the thermal Griffiths regions within the MBL phase have a fractal dimension $d_f < 1$ in these one-dimensional systems. This is a clear result of our RG, and the mechanism by which this happens seems like it might be more generally valid and not just an artifact of our approximations. One consequence of such fractal Griffiths regions is that averaged correlations and entanglement within eigenstates in the MBL phase can decay with distance x as stretched exponentials, $\sim \exp\left(-(x/x_0)^{d_f}\right)$, instead of the simple exponentials that one might naively expect.

Most results in this chapter are reported in the paper [72]. We will discuss our approximate RG in detail in Section 4.2. The fixed point distribution and the critical exponents for its stability will be calculated in Section 4.3 and Section 4.4. Section 4.5 is devoted to the fractal effect, and we will summarize this chapter in Section 4.6.

4.2 An Approximate RG

Now we present our approximate RG, pointing out and discussing the various assumptions and approximations that are used. We refer to the two previous RG studies as VHA [41] and PVP [54]. Like them, we consider a one-dimensional system whose dynamics is given by a local Hamiltonian, or more generally a local Floquet operator, with quenched randomness. The system has a MBL phase transition and the system's parameters are near this critical point. We assume, as in VHA, that each local region of this system can be classified either as thermalizing (T) or insulating (I). This need not be true of the system at the microscopic scale, but we are assuming that under coarse graining the critical point does flow to an infinite-randomness fixed point where such a "black and white" description is correct, and we have already coarse-grained enough for this to be a good approximation. This does happen within our RG (as well in both VHA and PVP), so this assumption is at least internally consistent. One question for future investigation is whether all these approximate RG's are possibly missing some important physics of the transition by not allowing for some intermediate local behaviors between fully thermalizing and fully insulating to be relevant at the critical fixed point.

If we have such a one-dimensional system and, as we assume, all regions of it can be classified as either T or I, then the system is a chain of "blocks" of various lengths that alternate along the chain between T and I. In the previous RG studies [41, 54], each such block was characterized by only two parameters: the typical many-body energy level spacing of the block, and some rate at which entanglement can spread from one end of the block to the other end. Our RG is even more "simplified" and characterizes each block only by whether it is T or I and by its many-body level spacing. The justifications for making this approximation of ignoring the precise value of the "entanglement rate" for each block are as follows. For almost all T blocks the entanglement rate at large ℓ is much larger than the level spacing which is exponen-

tially small with ℓ. As a consequence it is a reasonable approximation to ignore the precise magnitudes of these large T-block entanglement rates and just assume they are very fast compared to the many-body level spacing [70]. Near the critical point the I blocks at large ℓ are almost all near critical and have entanglement rates whose logarithms are close to that of the level spacing, so we make the approximation that the entanglement rate and the many-body level spacing are equal for each I block [70]. These are certainly oversimplifications, and we know that our RG does get some of the physics incorrect, as we discuss below. The virtues of our RG are its simplicity and that even with this simplicity it does appear to get some of the physics of the MBL transition qualitatively correct.

The many body level spacing of a one-dimensional block of length ℓ is $\sim \exp(-s\ell)$, where s is the entropy per unit length (e.g., $s = \log 2$ for a spin-1/2 chain at infinite temperature). We use the block's length ℓ as the parameter that quantifies its level spacing. The nth block in the chain has length ℓ_n. Once we have coarse-grained to a scale where adjacent blocks typically differ substantially in length, we can use a strong-randomness RG approach, justified by the typical ratio of many-body level spacings in two adjacent blocks being $\sim \exp(-s|\ell_n - \ell_{n+1}|) \ll 1$. Note that our RG, like the previous ones [41,54], assumes that the dynamic critical scaling is given by the many-body level spacing, which is consistent with numerical studies on a spin-chain model's dynamics near its MBL transition [13].

A single RG step is simply as follows: Find the shortest remaining block; say it is block n. This is the remaining block with the largest level spacing. Merge this block with its neighbor blocks on both sides to make a new larger block with length

$$\ell_{new} = \ell_{n-1} + \ell_n + \ell_{n+1} \ . \tag{4.1}$$

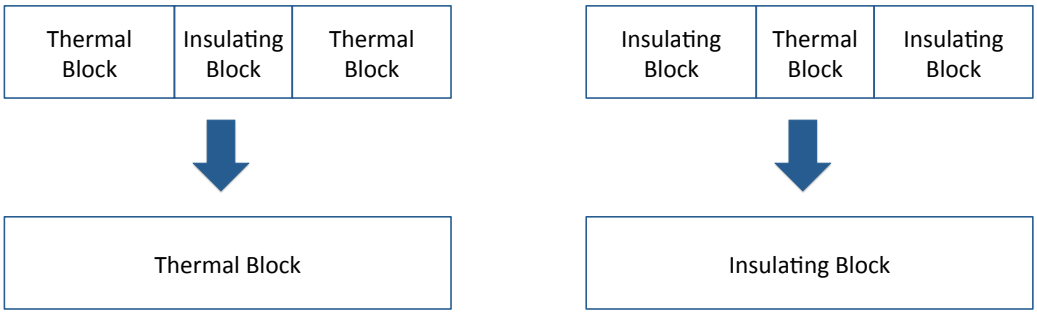

(a) TIT rule (b) ITI rule

Figure 4.1: A sketch of the RG rules. (a) shows the TIT rule where a central I (insulating) block is surrounded by two longer T (thermal) blocks, and after merging the new longer block is thermal. (b) shows the ITI move where a T block is surrounded by two longer I blocks and the resulting new block is insulating.

If the shortest block n is an I block, then the new longer block is a T block. A sketch of this "TIT" move is shown in Fig. 4.1(a). The neighbor blocks, both of which are T blocks that are longer than I block n, serve as local "baths" and thermalize the shorter central I block. This relies on the level spacings in both of the longer neighbor T blocks being much smaller than the rate of entanglement spread across the shorter central I block, so the two T blocks get strongly entangled across the I block. Thus it is quite plausible that the eigenstates of this new T block of length ℓ_{new}, isolated from its neighbors, are thermal, with thermal "volume-law" entanglement within this new block. In this case, where two longer T blocks thermalize a shorter I block, the approximations we make in our simple RG seem plausible near the MBL phase transition. It is for the other case, when block n is a T block, that we have to make some questionable assumptions to produce a simple RG.

If the shortest block n is a T block, then the two neighbor blocks are I blocks, and we assume the new longer block that is then made in this RG step is an I block. Fig. 4.1(b) illustrates this "ITI" rule. The two longer I blocks are isolating the shorter central T block from other T blocks, and thus localizing it. On one level

this seems sensible: the rate of entanglement spread across the neighbor I blocks is much smaller than the level spacing of the shorter central T block, so should not mix the eigenstates of the central block. But if we ask about the rate of entanglement spread across the new long I block of length ℓ_{new}, a reasonable estimate would be $\sim \exp\left(-s(\ell_{n-1} + \ell_{n+1})\right)$, since the spread across the central T block is assumed to be very fast. This suggests that our new long I block may not really be insulating, since this rate is much larger than its level spacing, but we will proceed with the assumption that this new block is indeed I.

One feature of this simple RG that makes it simple is that it is invariant on swapping I and T. This is because we are treating the process of two T blocks thermalizing a shorter central I block as mathematically the same as two I blocks localizing a shorter central T block. Unfortunately, we know that the real system does not have such a symmetry. Facilitating entanglement is very different from, and much "easier" than, blocking the spread of entanglement, because interacting quantum systems generically do get entangled. In the "battle" between thermalization and localization, thermalization always has "the upper hand". And we know from all the numerical studies of one-dimensional models that the properties of the phase transition are very asymmetric between the MBL phase and the thermal phase, with the critical point appearing very localized and the changes in systems' properties happening almost all on the thermal side of the phase transition (see, e.g., Refs. [41, 51, 54]).

Our approximate RG is mathematically equivalent to a domain coarsening model solved by Rutenberg and Bray [73] and Bray and Derrida [74]. The model they solved is a limiting case of deterministic zero-temperature domain coarsening in a classical one-dimensional system with short-range interactions and a nonconserved Ising-like order parameter. In this limit the shortest domain disappears first, allowing the two adjacent domains to grow, merge, and thus produce a new domain whose length is the sum of the lengths of the original three domains. Our RG is also similar to those

of Fisher for the ground states of certain disordered spin chains [75]. The difference from Fisher's RG is "simply" a sign: his RG can be written as $\ell_{new} = \ell_{n-1} - \ell_n + \ell_{n+1}$, where ℓ in this case is the logarithm of the renormalized interaction.

4.3 Critical Fixed Point Distribution

Due to the symmetry between T blocks and I blocks within our RG, the length distributions of these two types of blocks are identical at the critical fixed point. To derive the RG equations [73, 75], we define the length cutoff

$$\Lambda \equiv \min_n \ell_n \tag{4.2}$$

and

$$\zeta_n \equiv \ell_n - \Lambda \tag{4.3}$$

for a block of length ℓ_n, so $\zeta_n \geq 0$. The RG rule (4.1) becomes (giving the shortest block the label $n = 2$):

$$\zeta_{new} = \zeta_1 + \zeta_2 + \zeta_3 + 2\Lambda = \zeta_1 + \zeta_3 + 2\Lambda\,, \tag{4.4}$$

where $\zeta_2 = 0$ because the second block is at the cutoff: $\ell_2 = \Lambda$. Fisher's RG does not have the additive 2Λ term; it is instead $\zeta_{new} = \zeta_1 + \zeta_3$. This difference makes our fixed point rather different from Fisher's, although the same approach is used to write out the fixed point equation. A key point in both RGs is that the length of the new block only depends on the 3 blocks that are removed, so if the lengths of the blocks are initially uncorrelated, no correlations are generated by this RG [73, 75]. And any short-range correlations between block lengths are suppressed by the coarse-graining of the RG. Thus the fixed point distribution has the block lengths uncorrelated, so we only need to study the single-block length distribution.

The probability distribution of ζ at cutoff Λ is denoted as $\rho(\zeta, \Lambda)$. In order to treat the critical point we now assume both types of blocks have the same length distribution. At each RG step, when the cutoff Λ changes by $d\Lambda$, all the blocks with ζ in the interval $[0, d\Lambda]$ are removed and new blocks are formed by combining them with their two neighboring blocks. The distribution then needs to be re-normalized and shifted back to have $\zeta_{min} = 0$. These steps all combine to produce the integro-differential equation:

$$\frac{\partial \rho}{\partial \Lambda} = \frac{\partial \rho}{\partial \zeta} + \rho(0, \Lambda) \int_0^\infty d\zeta_a \int_0^\infty d\zeta_b \, \rho(\zeta_a, \Lambda) \rho(\zeta_b, \Lambda) \delta(\zeta - \zeta_a - \zeta_b - 2\Lambda) \, . \tag{4.5}$$

As the cutoff Λ gets large, the distribution of ζ becomes broad, and the system thus approaches an infinite-randomness fixed point. To treat that fixed point, we divide all lengths by the cutoff, thus keeping the rescaled length cutoff at one:

$$\eta \equiv \frac{\zeta}{\Lambda} \, , \qquad \rho(\zeta, \Lambda) \equiv \frac{1}{\Lambda} Q(\eta, \Lambda) = \frac{1}{\Lambda} Q(\frac{\zeta}{\Lambda}, \Lambda) \, . \tag{4.6}$$

$Q(\eta)$ is then invariant under the RG flow at the critical fixed point. We thus have the RG equation for the critical fixed point distribution $Q^*(\eta)$, independent of Λ, as:

$$\frac{d}{d\eta} \Big[(1 + \eta) Q^* \Big] + Q^*(0) \Theta(\eta - 2) \int_0^{\eta - 2} Q^*(\eta_a) Q^*(\eta - \eta_a - 2) d\eta_a = 0 \, . \tag{4.7}$$

As the total length of system is constant, $\sum_n \ell_n$ is also fixed. At the fixed point, this becomes

$$\sum_i \ell_i = \Lambda \sum_i (1 + \eta_i) = \Lambda N(\Lambda) \, (1 + \langle \eta \rangle_{f.p.}) \tag{4.8}$$

where $N(\Lambda)$ is the total number of blocks when the cutoff is Λ and $\langle \eta \rangle_{f.p.}$ is the average value of η at the fixed point, which is independent of Λ. This implies that the product ΛN is a constant, which results in $Q^*(0) = 1/2$, and this acts as a boundary condition for Eq. (4.7) so that it can be integrated out iteratively. In the interval

$0 \leq \eta \leq 2$, Eq. (4.7) is solved by

$$Q^*(\eta) = \frac{1}{2(1+\eta)}\,, \quad \text{for} \quad 0 \leq \eta \leq 2\,, \tag{4.9}$$

and using this expression, in the interval $2 \leq \eta \leq 4$ we have

$$Q^*(\eta) = \frac{1}{1+\eta}\Big[\frac{1}{2} - \int_2^{\eta} \frac{\ln(\eta'-1)}{4\eta'} d\eta'\Big]\,, \quad \text{for} \quad 2 \leq \eta \leq 4\,. \tag{4.10}$$

In principle, the analytical form of $Q^*(\eta)$ for any $\eta \geq 0$ can be obtained in the same way by treating $Q^*(\eta)$ in a piecewise manner. This shows that the physical (non-negative at all $\eta \geq 0$) solution to Eq. (4.7) is unique. The closed form solution for $Q^*(\eta)$ is shown in Rutenberg and Bray [73]. Asymptotically $Q^*(\eta)$ falls off exponentially: $Q^*(\eta) \sim C_Q \exp(-\lambda_Q \eta)$ for $\eta \gg 1$. The function is exhibited in Fig. 4.2.

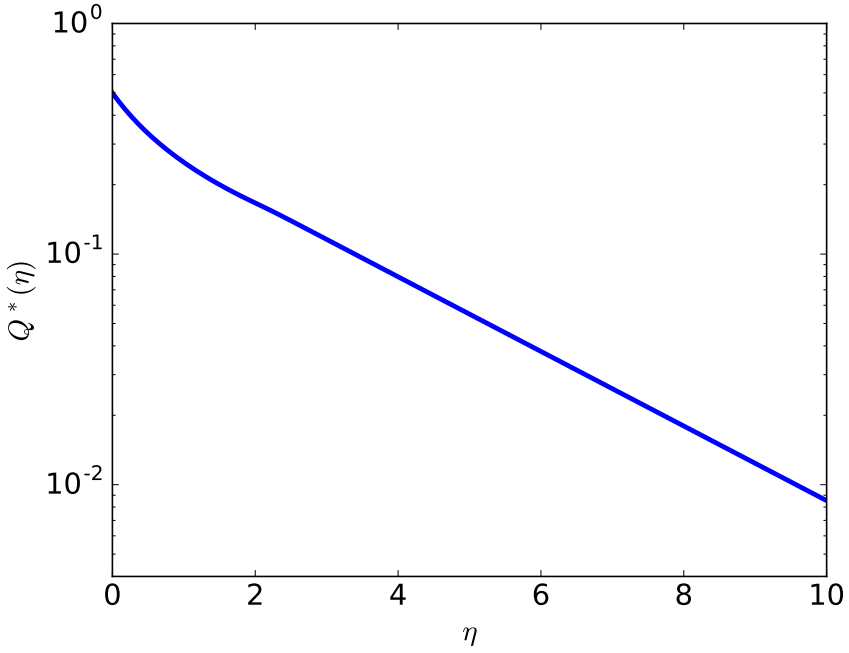

Figure 4.2: The scaled fixed point length distribution $Q^*(\eta)$.

4.4 Critical Exponents

By perturbing the distribution away from $Q^*(\eta)$, we can study the critical components related to the stability of this fixed point. Moving away from the critical point generates different distributions for T and I blocks: $Q_T(\eta,\Lambda)$ and $Q_I(\eta,\Lambda)$, and when the critical fixed point is unstable under this perturbation, the difference grows as the RG flows, driving the system into either the thermal phase or the localized phase. Similar to the derivation of $Q^*(\eta)$, the RG equations for these two distributions can be found as

$$\begin{cases} \Lambda\dfrac{\partial Q_T}{\partial\Lambda} = Q_T + (1+\eta)\dfrac{\partial Q_T}{\partial\eta} + Q_T(\eta,\Lambda)\Big[Q_T(0,\Lambda) - Q_I(0,\Lambda)\Big] \\ \qquad\qquad + Q_I(0,\Lambda)\Theta(\eta-2)\displaystyle\int_0^{\eta-2} d\eta_a\, Q_T(\eta_a,\Lambda)Q_T(\eta-\eta_a-2,\Lambda)\,; \\ \Lambda\dfrac{\partial Q_I}{\partial\Lambda} = Q_I + (1+\eta)\dfrac{\partial Q_I}{\partial\eta} + Q_I(\eta,\Lambda)\Big[Q_I(0,\Lambda) - Q_T(0,\Lambda)\Big] \\ \qquad\qquad + Q_T(0,\Lambda)\Theta(\eta-2)\displaystyle\int_0^{\eta-2} d\eta_a\, Q_I(\eta_a,\Lambda)Q_I(\eta-\eta_a-2,\Lambda)\,. \end{cases} \tag{4.11}$$

To investigate the critical exponents, we consider a small perturbation away from $Q^*(\eta)$:

$$\begin{cases} Q_T(\eta,\Lambda) \equiv Q^*(\eta) + \delta_T(\eta,\Lambda)\,, \\ Q_I(\eta,\Lambda) \equiv Q^*(\eta) + \delta_I(\eta,\Lambda)\,, \end{cases} \tag{4.12}$$

and for $Q_{T,I}$ to still be probability distributions, $\delta_{T,I}$ both must satisfy

$$\int_0^\infty \delta_{T,I}(\eta,\Lambda)d\eta = 0\ . \tag{4.13}$$

For simplicity in calculation, we further define

$$\begin{cases} \delta_+(\eta,\Lambda) \equiv \delta_T(\eta,\Lambda) + \delta_I(\eta,\Lambda)\,, \\ \delta_-(\eta,\Lambda) \equiv \delta_T(\eta,\Lambda) - \delta_I(\eta,\Lambda)\,, \end{cases} \tag{4.14}$$

so to linear order, the equations for δ_+ and δ_- are

$$\Lambda\frac{\partial\delta_+}{\partial\Lambda} = \delta_+ + (1+\eta)\frac{\partial\delta_+}{\partial\eta} + \delta_+(0,\Lambda)\Theta(\eta-2)\int_0^{\eta-2} d\eta_a\, Q^*(\eta_a)Q^*(\eta-\eta_a-2) + \Theta(\eta-2)\int_0^{\eta-2} d\eta_a\, \delta_+(\eta_a,\Lambda)Q^*(\eta-\eta_a-2) \tag{4.15}$$

and

$$\begin{aligned}\Lambda\frac{\partial\delta_-}{\partial\Lambda} =& \delta_- + (1+\eta)\frac{\partial\delta_-}{\partial\eta} + 2Q^*(\eta)\delta_-(0,\Lambda) \\ &- \delta_-(0,\Lambda)\Theta(\eta-2)\int_0^{\eta-2} d\eta_a\, Q^*(\eta_a)Q^*(\eta-\eta_a-2) \\ &+ \Theta(\eta-2)\int_0^{\eta-2} d\eta_a\, \delta_-(\eta_a,\Lambda)Q^*(\eta-\eta_a-2)\,.\end{aligned} \tag{4.16}$$

To find the eigenmodes of the RG flow at the critical fixed point, we set

$$\begin{cases} \delta_+(\eta,\Lambda) \equiv \Lambda^{1/\nu_+} f_+(\eta)\,, \\ \delta_-(\eta,\Lambda) \equiv \Lambda^{1/\nu_-} f_-(\eta)\ . \end{cases} \tag{4.17}$$

Under this standard scaling assumption, we have

$$\frac{1}{\nu_+}f_+(\eta) = f_+(\eta) + (1+\eta)\frac{df_+}{d\eta} + f_+(0)\Theta(\eta-2)\int_0^{\eta-2} d\eta_a\, Q^*(\eta_a)Q^*(\eta-\eta_a-2) + \Theta(\eta-2)\int_0^{\eta-2} d\eta_a\, f_+(\eta_a)Q^*(\eta-\eta_a-2)\,. \tag{4.18}$$

and

$$\begin{aligned}\frac{1}{\nu_-}f_-(\eta) =& f_-(\eta) + (1+\eta)\frac{df_-}{d\eta} + 2Q^*(\eta)f_-(0) \\ &- f_-(0)\Theta(\eta-2)\int_0^{\eta-2} d\eta_a\, Q^*(\eta_a)Q^*(\eta-\eta_a-2) \\ &+ \Theta(\eta-2)\int_0^{\eta-2} d\eta_a\, f_-(\eta_a)Q^*(\eta-\eta_a-2)\,.\end{aligned} \tag{4.19}$$

The critical exponents can then be found as eigenvalues of these two equations. Note that the solutions also need to satisfy the normalization constraint from Eq. (4.13):

$$\int_0^\infty f_\pm(\eta)d\eta = 0 \ . \tag{4.20}$$

On the other hand, integrating both sides of Eqs. (4.18) and (4.19) gives

$$\Big(\frac{1}{\nu_\pm} - 1\Big)\int_0^\infty f_\pm(\eta)d\eta = 0 \tag{4.21}$$

assuming both integrations exist. Therefore the normalization constraint is automatically satisfied if the eigenvalue is not 1; otherwise we do need to check the normalization.

We diagonalized these two eigenvalue equations numerically. The derivative was discretized to second order as a right derivative to make it well-behaved even at $\eta = 0$ where the functions do not exist to the left (for $\eta < 0$), and the integration was discretized with the trapezoidal rule. For f_+ all eigenfunctions corresponding to the largest eigenvalue of 1 are of the same sign and so are not normalizable and are thus unphysical. The second largest eigenvalue has a real part of about -4.4. This shows that δ_+ decays at least as fast as $\sim \Lambda^{-4.4}$ when the RG is flowing and therefore is irrelevant and associated with the flow on the critical manifold toward the fixed point distribution. This shows that the fixed point distribution $Q^*(\eta)$ is stable if Q_T and Q_I are perturbed in the same direction.

For f_-, again the eigenvalue with the largest real part is $\frac{1}{\nu_-} = 1$ and its corresponding eigenfunction cannot be normalized and so is unphysical. The eigenvalue with the second largest real part is positive and real and is the critical exponent we are looking for. Fig. 4.3(a) and Fig. 4.3(b) show our estimates of $1/\nu_-$ at different η_{max} and Δ_f. It can be seen that the results converge well when η_{max} is increased and Δ_f is decreased, and when $\Delta_f = 0.005$ and $\eta_{max} = 40$, we have $1/\nu_- \approx 0.3994$ which

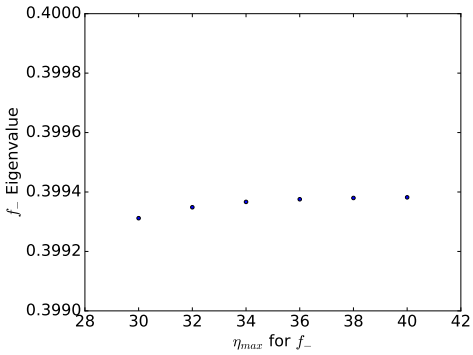

(a) $1/\nu_-$ at different η_{max}

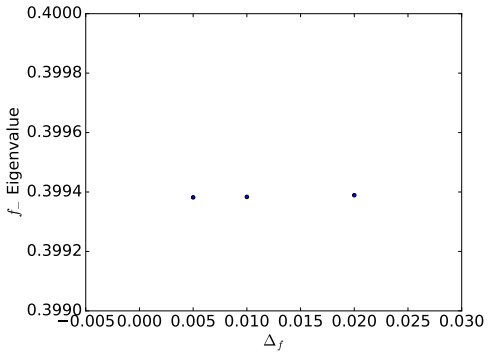

(b) $1/\nu_-$ at different Δ_f

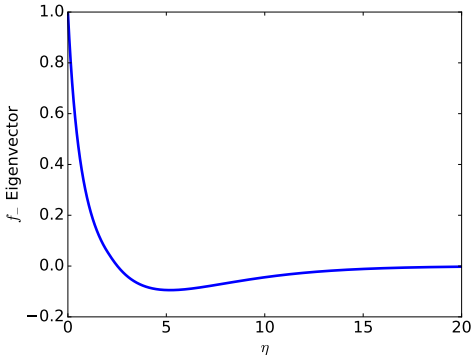

(c) $f_-(\eta)$

Figure 4.3: The eigenvalue $1/\nu_-$ and eigenfunction $f_-(\eta)$ from numerical diagonalization: (a) shows the eigenvalues at different η_{max} with $\Delta_f = 0.005$. (b) shows the eigenvalues at different Δ_f with $\eta_{max} = 40$. (c) gives the corresponding eigenvector at $\Delta_f = 0.005$ and $\eta_{max} = 40$.

matches what was obtained by Bray and Derrida [74]. The next eigenvalue after that has a negative real part $\cong -1.8$, so as expected there is only one physical relevant operator at this critical fixed point. The corresponding eigenfunction is shown in Fig. 4.3(c) with $f_-(0)$ normalized to 1. The numerical integration of it using trapezoidal rule gives about -0.0001, which confirms the constraint $\int_0^\infty f_-(\eta) = 0$ to the numerical precision we used. Since this critical exponent is positive, the fixed point distribution is unstable against this perturbation which drives Q_T and Q_I in opposite directions and the system thus flows away from criticality into either the thermal or the MBL phase. The difference grows as $\sim \Lambda^{1/\nu_-}$ as the length cutoff increases.

Note that this $\nu_- \cong 2.50$ satisfies and does not saturate the Chayes inequality [64, 69], which in this case of $d = 1$ is $\nu_- \geq 2$. This is qualitatively the same as the previous RGs [41, 54], although this value of ν_- is quantitatively a little smaller than those of VHA and PVP. Some good understanding of "why" this exponent exceeds the Chayes bound still eludes us.

4.5 Fractal Griffith Regions

As the RG flows away from the critical fixed point into one of the phases, the two length distributions become very different in width. If we flow into the thermal phase the chain becomes mostly T, with the remaining I blocks being rare and almost all of length very close to the length cutoff. The T blocks get an arbitrarily broad length distribution, with almost all T blocks much longer than the cutoff. Since almost all blocks of length near the cutoff are I blocks, almost all RG moves are TIT moves and make the already long T blocks even longer; our RG seems like a safe approximation for these moves. However some small fraction of the RG moves are ITI moves with the three blocks all being of length near the cutoff. These are the moves that maintain the population of rare I blocks (the Griffiths regions), but these are precisely the type of RG moves for which our RG approximations are not to be trusted, as we discuss above. Thus we do not expect our approximate RG to correctly model the Griffiths regions of rare insulating segments in the thermal phase, even qualitatively. We will return to this after examining the Griffiths regions in the MBL phase.

As the RG flows from near the critical fixed point to "deep" in the MBL phase, it goes into the MBL regime where almost all RG moves are ITI moves that make the already long I blocks even longer. For these moves, our RG is typically a good approximation, because the T block that is "integrated out" is typically much shorter than the two adjacent I blocks, so effectively we are just joining two very long I blocks

to make an even longer I block. However, occasionally there remains a rare short I block with length at the cutoff that is slightly shorter than its adjacent T blocks, and it produces a TIT move and allows the rare T blocks to grow, thus generating the Griffiths regions, which are rare long T blocks within the MBL phase. For these moves, our RG seems like a reasonable approximation: the two T blocks get entangled with each other across the short I block between them.

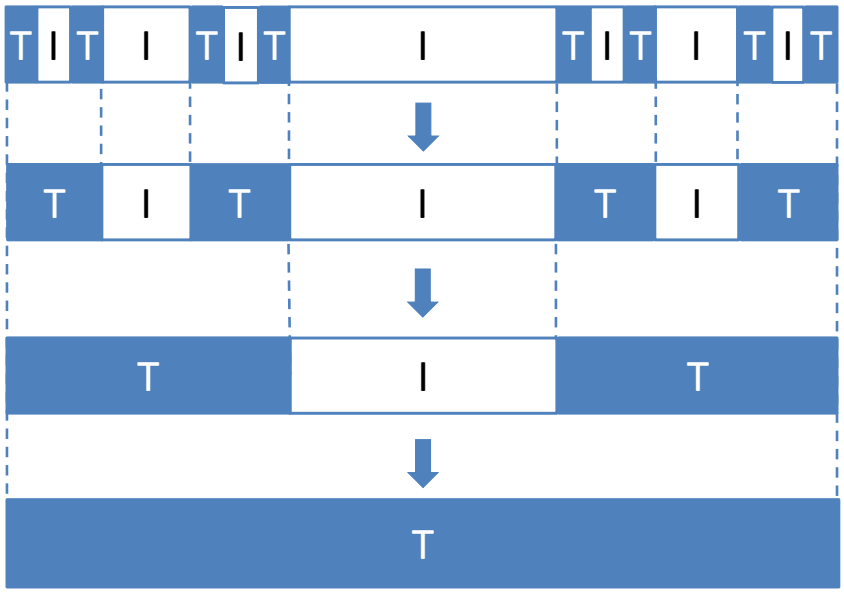

Figure 4.4: A sketch of part of the fractal structure of a rare large Griffiths T (locally thermalizing) region in the MBL phase.

Now let us ask what is the most probable way that our RG makes a large T Griffiths block within the MBL phase near the transition. This is illustrated in Fig 4.4. The large T block arose from a TIT move. In this limit where the RG has flowed from near the critical point to "deep" within the MBL phase, almost all T blocks have lengths near the cutoff, so in this TIT move, the I block's length is at the cutoff and the two T blocks most likely have lengths just above the cutoff, so all three blocks are of essentially the same length. The I block can be typical, so it

typically arose much earlier in the RG by integrating out a very short T block. The T blocks are themselves rare and each arose when the cutoff length was roughly 3 times shorter from similar TIT moves. Thus we see that within this RG these Griffiths regions are generated from a fractal set of rare T blocks that, on scales much smaller than the final rare T block, happened to be placed just correctly such that they are able, within this approximate RG, to thermalize all the intervening typical I blocks. This fractal set of rare T blocks has fractal dimension $d_f = \log 2/\log 3 \cong 0.631$ in the limit of the largest such Griffiths regions.

We can also formulate RG equations for d_f exactly at the critical point as in Ref. [75] so that we can obtain d_f at the transition point to numeric precision. To do so, we first define a length ℓ_T in a thermal block to be the total length of fractal thermal parts inside it as shown in Fig. 4.4. With this definition, effectively $\ell_T = 0$ inside an insulating block and at each RG step, we have extra RG rules as $\ell_T' = \ell_{Tn-1} + \ell_{Tn+1}$ when the central block n is insulating and $\ell_T' = 0$ otherwise. In general, $\ell_T \sim \ell^{d_f}$ for a thermal block of length ℓ and $d_f < 1$ represents a fractal structure. To incorporate ℓ_T into RG equations, we need to redefine Q_T to include another variable representing ℓ_T. Analog to the treatment of magnetic moments in Fisher [75], we define

$$\gamma = \ell_T/\Lambda^{d_f} \geq 0 \tag{4.22}$$

where Λ is defined in Eq. (4.2), so now we have new scaled probability distribution $Q_T(\eta, \gamma)$ while Q_I is the same as before. The RG equation for Q_T^* at the critical point is then

$$\begin{aligned}&\frac{\partial}{\partial\eta}\big[(1+\eta)Q_T^*(\eta,\gamma)\big] + d_f\frac{\partial}{\partial\gamma}\big[\gamma Q_T^*(\eta,\gamma)\big] \\ &+ \frac{1}{2}\Theta(\eta-2)\int_0^{\eta-2}\int_0^{\gamma} Q_T^*(\eta_1,\gamma_1)Q_T^*(\eta-\eta_1-2,\gamma-\gamma_1)d\eta_1 d\gamma_1 = 0\end{aligned} \tag{4.23}$$

whereas that of Q_I^* remains the same. Note $\int_0^\infty Q_T^*(\eta,\gamma)d\gamma = Q^*(\eta)$ gives back the critical distribution calculated in Section 4.3. To cast Eq. (4.23) into a more tractable form, we further define

$$g(\eta) = \int_0^\infty \gamma Q_T^*(\eta,\gamma)d\gamma\,. \tag{4.24}$$

The integration is expected to exist, since the conditional expectation of γ, $C(\eta) = g(\eta)/Q^*(\eta)$, is expected to exist for all η. Moreover, analog to the treatment of magnetic moments in Fisher [75], $C(\eta)$ is expected to follow a power law at large η, so asymptotically $g(\eta) \sim \eta^\beta \exp(-\lambda_Q \eta)$. Eq. (4.23) implies that

$$(1-d_f)g(\eta) + (1+\eta)\frac{dg}{d\eta} + \Theta(\eta-2)\int_0^{\eta-2} g(\eta_1)Q^*(\eta-\eta_1-2)d\eta_1 = 0 \tag{4.25}$$

and this equation gives $\beta = 1$ from asymptotic analysis. Finding d_f at the critical point then becomes an eigenvalue problem which can be solved numerically as in Section 4.4. Here η were sampled with spacing Δ_g from 0 up to η_{max}. Fig. 4.5 illustrates the numerical results. They demonstrate that our results converge very well when η_{max} is increased and Δ_g is decreased, and suggest that $d_f \approx 0.8249 < 1$ so we are indeed looking at a fractal structure at the transition point. This numerical value itself, however, is likely to be less reliable than the one near the transition point in the MBL phase, as the ITI moves become more questionable when we approach from the MBL phase to the thermal phase.

The above fractal dimension d_f can be examined numerically. Particularly, the conditional expectation of ℓ_T at the cutoff follows

$$r(\Lambda) = \ln\big(E[\ell_T|\eta=0]\big) = d_f \ln\Lambda + \ln C(0,\Lambda) \tag{4.26}$$

where $C(\eta,\Lambda)$ is the conditional expectation of γ at a given η, which would be independent of Λ at a fixed point. Therefore d_f can be obtained by plotting $r(\Lambda)$

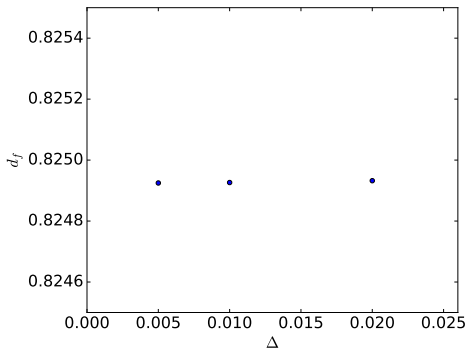

(a) d_f at changing η_{max}

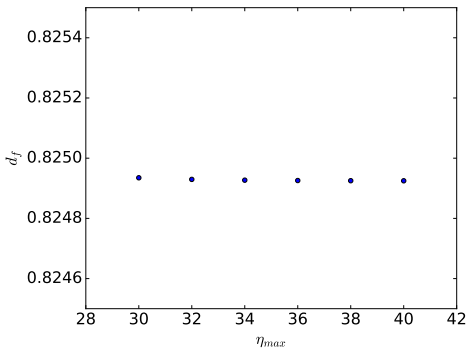

(b) d_f at changing Δ_f

Figure 4.5: The eigenvalue d_f from numerical diagonalization of equation Eq. (4.25). (a) shows d_f at different η_{max} with $\Delta_g = 0.005$. (b) shows d_f at different Δ_g with $\eta_{max} = 40$.

against Λ, which can be constructed by recording a T block's length $\ell = \Lambda$ and ℓ_T when it is decimated. At the critical point, we can use the numerical $Q^*(\eta)$ as the starting distribution to simulate the RG flow. It is found that (not shown here) $d_f \approx 0.829 \pm 0.006$ at the critical point, thus in agreement with the analytic approach $d_f \approx 0.8249$. We can also test d_f in the Griffith regions with initial length distributions $Q_T(\eta) = \mathrm{e}Q^*(\mathrm{e}\eta)$ and $Q_I(\eta) = Q^*(\eta/\mathrm{e})/\mathrm{e}$, so we start near the transition and flow away into the MBL phase. After a short transient, it is found the results approach the expected $L_T \sim L^{d_f}$, with $d_f = 0.635 \pm 0.03$, quite consistent with the expected fractal dimension.

In our simplified RG, we work only near the critical point, where the entanglement rate across an I block is close to the block's many-body level spacing. If the bare system is actually farther into the MBL phase away from the critical point, then the entanglement rate across a typical I block will decay with block length faster than the many-body level spacing, and when we grow a fractal Griffiths region using TIT moves (in a less simplified RG such as VHA [41]) and typical I blocks, then for the two T blocks to become entangled, the I block needs to be shorter than the two T blocks and as a result its fractal dimension d_f will be larger, with $\log 2/\log 3 < d_f < 1$. In

the limit where the bare system is deep in the MBL phase d_f approaches unity, and d_f decreases as the transition is approached.

If this proposal of fractal Griffiths regions within the MBL phase in one dimension is not just an artifact of the approximations we make, there seem to be at least two possible scenarios: One possibility is that the result is only partially correct: the microscopic T blocks within the fractal Griffiths region do get entangled with each other, but they do not succeed in becoming strongly entangled with, and thus locally thermalizing, the typical I blocks that are in between them within the Griffiths region. In this case, there will be resulting correlations and entanglement within the many-body eigenstates that extend across the Griffiths regions, so extend to distance ℓ with a probability that falls off as a stretched exponential function of ℓ. But the effective many-body level spacing of this Griffiths region may be set not by the full length of the region, but only by the length $\sim \ell^{d_f}$ that is within the entangled T blocks on the microscopic scale. This is the scenario that was mentioned and assumed in Ref. [59]. The other possibility is that the Griffiths regions are fully thermal and entangled, and they respond dynamically like they have a many-body level spacing set by their full length ℓ. In this case the result of Ref. [59] is modified so the spatially averaged low-frequency conductivity $\sigma(\omega)$ behaves instead as $\log(\sigma(\omega)/\omega) \sim -|\log\omega|^{d_f}$. Since d_f is not much less than one, for small system data this will be hard to distinguish from the continuously varying power of ω that arises [59] from the first scenario. However it would be a modification to the conclusions of Ref. [59], so that the Griffiths regions always dominate over the Mott many-body resonances in the limiting low-frequency conductivity of an infinite system.

Our simplified RG of course also gives fractal insulating Griffiths regions in the thermal phase, by symmetry. But this is almost certainly an artifact of the oversimplifications of this RG: A low density fractal of well-placed rare insulating regions is not capable of changing an otherwise typical thermal region into an insulator. Thus

our results do not suggest that a revision of the discussions [41, 56, 65] of Griffiths effects within the thermal phase is needed.

4.6 Conclusions

In this chapter we introduced a simplified RG for the MBL phase transition in one-dimensional systems. It is mathematically equivalent to an exactly solved domain coarsening model [73, 74], so the critical fixed point distribution and the critical exponents that characterize the stability of the critical point within our RG are known analytically or to numerical precision. Even though some over-simplifications are incorporated to achieve this tractability, our approximate RG may correctly capture some qualitative features of the phase transition and of the MBL phase, and might provide a basis for future more systematic RG studies. One particular feature of this RG that we discussed in some detail is the fractal thermal Griffiths regions within the MBL phase that it produces, which seem like they might be a qualitatively correct feature of MBL in one dimension with quenched randomness.

Chapter 5

Conclusion

In this thesis we have discussed our studies on thermalization and the many-body phase transition between the localized phase and the thermal phase. The investigation of thermalization process under quantum theory started at the foundation of quantum mechanics, but the details of the dynamical process still eludes our understanding. A particular interesting topic in this area recently is the many-body localized systems where the thermalization fails. The transition of thermalized systems into the localized phase is an eigenstate phase transition that waits further exploration.

In Chapter 2, we studied the influence of conservation laws on thermalization of entanglement. We focused our numerical studies on two one-dimensional spin chains and examined our results between a Hamiltonian model which is robustly non-integrable and a Floquet model which has no conservation laws. The energy conservation for the Hamiltonian model restricts its eigenstates, thus they appear less thermalized at finite size than those of the Floquet model. By studying dynamics of von Neumann entanglement entropy from different initial states, it is found that the energy conservation slows down the thermalization of entanglement, which we attribute to the slow diffusive transport of energy imbalances across the spin chain

under the conservation law. We further found that under Hamiltonian dynamics, a larger energy imbalance initially leads to slower entropy dynamics, and similar results also apply to relaxation of entropy fluctuations. We examined the dynamics of the energy imbalance with the longest wavelength, i.e., the variance of energy difference between left and right half chains $\langle (H_R - H_L)^2 \rangle$, and found that in most cases it is directly correlated with the dynamics of entropies, which is consistent with our qualitative observation, but exceptions do exist. Therefore to have a more thorough understanding of the thermalization of entanglement under energy conservation, a more careful analysis of the transport of energy imbalance under quantum mechanics is needed.

In Chapter 3, we turned our attention to the many-body localization phase transition and proposed a Floquet model for numeric studies. Since if Floquet systmes thermalize, their eigenstates appear to thermalize better at finite size than those of Hamiltonian systems, this model may aid us in obtaining more accurate numeric results as the transition point is located in the thermal phase at finite size. We checked some popular quantities for our Floquet model, and they confirmed that it indeed has a well thermalized region and a well localized region at reasonable system sizes. We specifically looked at two correlation functions involving the spins at two ends of the spin chain. They are expected to display peaks at the transition point, but the peaks were difficult to observe in Hamiltonian systems at small sizes while much more obvious in our Floquet model. We attempted a preliminary finite size analysis of the correlations at different system sizes and with different spin separations. The results were qualitatively promising, but to be statistically more accurate we certainly need to go to larger systems with more realizations of disorder configurations, which can be a future research project.

In Chapter 4, we investigated the many-body localization phase transition using a simplified renormalization group (RG) approach, which we hope can serve as basis for

further more complete RG treatments. Under coarse graining, we divided the system into regions which are either thermal or localized, and the RG rules are symmetric of both, which is not an accurate description of the whole system, but we hope it can capture some physics qualitatively correct near the fixed point and it also makes the mathematics tractable. This approximate RG is mathematically equivalent to a domain coarsening model [73, 74] whose fixed point distribution and stability critical exponents can be found analytically or to numeric precision. We also constructed a fractal structure whose fractal dimension can be found at the critical point and "deep" in the localized region near the fixed point, and it may affect the Griffith regions near transition.

Thermalization and many-body localization are rich subjects with many interesting and far-reaching topics to explore. The results presented in the thesis have only just scratched the surfaces of these colossal buildings, and hopefully they can provide some insights into future research.

Bibliography

[1] L. D'Alessio and M. Rigol, Phys. Rev. X **4**, 041048 (2014).

[2] R. Nandkishore and D. A. Huse, Annual Review of Condensed Matter Physics **6**, 15 (2015).

[3] A. Polkovnikov, K. Sengupta, A. Silva, and M. Vengalattore, Rev. Mod. Phys. **83**, 863 (2011).

[4] J. M. Deutsch, Phys. Rev. A **43**, 2046 (1991).

[5] M. Srednicki, Phys. Rev. E **50**, 888 (1994).

[6] H. Tasaki, Phys. Rev. Lett. **80**, 1373 (1998).

[7] M. Rigol, V. Dunjko, and M. Olshanii, Nature **452**, 854 (2008).

[8] M. Rigol and M. Srednicki, Phys. Rev. Lett. **108**, 110601 (2012).

[9] M. Rigol, V. Dunjko, V. Yurovsky, and M. Olshanii, Phys. Rev. Lett. **98**, 050405 (2007).

[10] E. T. Jaynes, Phys. Rev. **106**, 620 (1957).

[11] A. C. Cassidy, C. W. Clark, and M. Rigol, Phys. Rev. Lett. **106**, 140405 (2011).

[12] J.-S. Caux and F. H. L. Essler, Phys. Rev. Lett. **110**, 257203 (2013).

[13] A. Pal and D. A. Huse, Phys. Rev. B **82**, 174411 (2010).

[14] M. Rigol, Phys. Rev. Lett. **103**, 100403 (2009).

[15] M. Rigol and L. F. Santos, Phys. Rev. A **82**, 011604 (2010).

[16] T. N. Ikeda, Y. Watanabe, and M. Ueda, Phys. Rev. E **87**, 012125 (2013).

[17] S. Dubey, L. Silvestri, J. Finn, S. Vinjanampathy, and K. Jacobs, Phys. Rev. E **85**, 011141 (2012).

[18] R. Steinigeweg, J. Herbrych, and P. Prelovšek, Phys. Rev. E **87**, 012118 (2013).

[19] A. De Luca, ArXiv e-prints (2013), 1302.0992.

[20] W. Beugeling, R. Moessner, and M. Haque, Phys. Rev. E **89**, 042112 (2014).

[21] R. Steinigeweg, A. Khodja, H. Niemeyer, C. Gogolin, and J. Gemmer, Phys. Rev. Lett. **112**, 130403 (2014).

[22] S. Khlebnikov and M. Kruczenski, ArXiv e-prints (2013), 1312.4612.

[23] M. P. Müller, E. Adlam, L. Masanes, and N. Wiebe, Communications in Mathematical Physics **340**, 499 (2015).

[24] P. W. Anderson, Phys. Rev. **109**, 1492 (1958).

[25] D. Basko, I. Aleiner, and B. Altshuler, Annals of Physics **321**, 1126 (2006).

[26] V. Oganesyan and D. A. Huse, Phys. Rev. B **75**, 155111 (2007).

[27] P. Calabrese and J. Cardy, J. Stat. Mech **2005**, P04010 (2005).

[28] G. D. Chiara, S. Montangero, P. Calabrese, and R. Fazio, J. Stat. Mech **2006**, P03001 (2006).

[29] T. Hartman and J. Maldacena, Journal of High Energy Physics **5**, 14 (2013), 1303.1080.

[30] H. Kim and D. A. Huse, Phys. Rev. Lett. **111**, 127205 (2013).

[31] C. K. Burrell and T. J. Osborne, Phys. Rev. Lett. **99**, 167201 (2007).

[32] M. Žnidarič, T. c. v. Prosen, and P. Prelovšek, Phys. Rev. B **77**, 064426 (2008).

[33] F. Iglói, Z. Szatmári, and Y.-C. Lin, Phys. Rev. B **85**, 094417 (2012).

[34] J. H. Bardarson, F. Pollmann, and J. E. Moore, Phys. Rev. Lett. **109**, 017202 (2012).

[35] R. Vosk and E. Altman, Phys. Rev. Lett. **110**, 067204 (2013).

[36] M. Serbyn, Z. Papić, and D. A. Abanin, Phys. Rev. Lett. **110**, 260601 (2013).

[37] M. Serbyn, Z. Papić, and D. A. Abanin, Phys. Rev. Lett. **111**, 127201 (2013).

[38] D. A. Huse, R. Nandkishore, and V. Oganesyan, Phys. Rev. B **90**, 174202 (2014).

[39] L. Amico, A. Osterloh, F. Plastina, R. Fazio, and G. Massimo Palma, Phys. Rev. A **69**, 022304 (2004).

[40] H. Liu and S. J. Suh, Phys. Rev. Lett. **112**, 011601 (2014).

[41] R. Vosk, D. A. Huse, and E. Altman, Phys. Rev. X **5**, 031032 (2015).

[42] M. C. Bañuls, J. I. Cirac, and M. B. Hastings, Phys. Rev. Lett. **106**, 050405 (2011).

[43] L. Zhang, H. Kim, and D. A. Huse, Phys. Rev. E **91**, 062128 (2015).

[44] H. Kim, T. N. Ikeda, and D. A. Huse, Phys. Rev. E **90**, 052105 (2014).

[45] A. B. Zamolodchikov, International Journal of Modern Physics A **04**, 4235 (1989).

[46] D. N. Page, Phys. Rev. Lett. **71**, 1291 (1993).

[47] A. Lazarides, A. Das, and R. Moessner, ArXiv e-prints (2014), 1403.2946v1.

[48] P. Ponte, A. Chandran, Z. Papić, and D. A. Abanin, Annals of Physics **353**, 196 (2015).

[49] H. Kim, M. C. Bañuls, J. I. Cirac, M. B. Hastings, and D. A. Huse, Phys. Rev. E **92**, 012128 (2015).

[50] C. Monthus and T. Garel, Phys. Rev. B **81**, 134202 (2010).

[51] J. A. Kjäll, J. H. Bardarson, and F. Pollmann, Phys. Rev. Lett. **113**, 107204 (2014).

[52] Y. Bar Lev and D. R. Reichman, Phys. Rev. B **89**, 220201 (2014).

[53] E. Altman and R. Vosk, Annual Review of Condensed Matter Physics **6**, 383 (2015).

[54] A. C. Potter, R. Vasseur, and S. A. Parameswaran, Phys. Rev. X **5**, 031033 (2015).

[55] M. Serbyn, Z. Papić, and D. A. Abanin, Phys. Rev. X **5**, 041047 (2015).

[56] K. Agarwal, S. Gopalakrishnan, M. Knap, M. Müller, and E. Demler, Phys. Rev. Lett. **114**, 160401 (2015).

[57] D. J. Luitz, N. Laflorencie, and F. Alet, Phys. Rev. B **91**, 081103 (2015).

[58] E. J. Torres-Herrera and L. F. Santos, Phys. Rev. B **92**, 014208 (2015).

[59] S. Gopalakrishnan *et al.*, Phys. Rev. B **92**, 104202 (2015).

[60] T. Devakul and R. R. P. Singh, Phys. Rev. Lett. **115**, 187201 (2015).

[61] J. Goold *et al.*, Phys. Rev. B **92**, 180202 (2015).

[62] W. De Roeck, F. Huveneers, M. Müller, and M. Schiulaz, Phys. Rev. B **93**, 014203 (2016).

[63] M. Serbyn and J. E. Moore, Phys. Rev. B **93**, 041424 (2016).

[64] A. Chandran, C. R. Laumann, and V. Oganesyan, ArXiv e-prints (2015), 1509.04285.

[65] S. Gopalakrishnan, K. Agarwal, E. Demler, D. A. Huse, and M. Knap, ArXiv e-prints (2015), 1511.06389.

[66] M. Serbyn, Z. Papić, and D. A. Abanin, Phys. Rev. Lett. **111**, 127201 (2013).

[67] A. Lazarides, A. Das, and R. Moessner, Phys. Rev. Lett. **115**, 030402 (2015).

[68] B. Bauer and C. Nayak, Journal of Statistical Mechanics: Theory and Experiment **2013**, P09005 (2013).

[69] J. T. Chayes, L. Chayes, D. S. Fisher, and T. Spencer, Phys. Rev. Lett. **57**, 2999 (1986).

[70] B. Zhao, *Eigenstate phase transitions*, PhD thesis, Princeton University, 2015.

[71] D. A. Huse, R. Nandkishore, V. Oganesyan, A. Pal, and S. L. Sondhi, Phys. Rev. B **88**, 014206 (2013).

[72] L. Zhang, B. Zhao, T. Devakul, and D. A. Huse, Phys. Rev. B **93**, 224201 (2016).

[73] A. D. Rutenberg and A. J. Bray, Phys. Rev. E **50**, 1900 (1994).

[74] A. J. Bray and B. Derrida, Phys. Rev. E **51**, R1633 (1995).

[75] D. S. Fisher, Phys. Rev. B **50**, 3799 (1994).